



HAL
open science

Multi-scale structural alterations of the thalamus and basal ganglia in focal epilepsy using 7T MRI

Roy Am Haast, Benoit Testud, Julia Makhalova, Hugo Dary, Alexandre Cabane, Arnaud Le Troter, Jean-philippe Ranjeva, Fabrice Bartolomei, Maxime Guye

► To cite this version:

Roy Am Haast, Benoit Testud, Julia Makhalova, Hugo Dary, Alexandre Cabane, et al.. Multi-scale structural alterations of the thalamus and basal ganglia in focal epilepsy using 7T MRI. *Human Brain Mapping*, 2023, 44 (13), pp.4754-4771. 10.1002/hbm.26414 . hal-04273665

HAL Id: hal-04273665









<https://hal.science/hal-04273665>

Submitted on 22 Apr 2024

HAL is a multi-disciplinary open access archive for the deposit and dissemination of scientific research documents, whether they are published or not. The documents may come from teaching and research institutions in France or abroad, or from public or private research centers.

L'archive ouverte pluridisciplinaire **HAL**, est destinée au dépôt et à la diffusion de documents scientifiques de niveau recherche, publiés ou non, émanant des établissements d'enseignement et de recherche français ou étrangers, des laboratoires publics ou privés.

Multi-scale structural alterations of the thalamus and basal ganglia in focal epilepsy using 7T MRI

Roy A. M. Haast^{1,2}  | Benoit Testud^{1,2}  | Julia Makhalova^{1,2,3}  |
 Hugo Dary^{1,2}  | Alexandre Cabane^{1,2} | Arnaud Le Troter^{1,2}  |
 Jean-Philippe Ranjeva^{1,2}  | Fabrice Bartolomei^{3,4}  | Maxime Guye^{1,2,3} 

¹Aix-Marseille Univ, CRMBM, CNRS UMR 7339, Marseille, France

²APHM, La Timone Hospital, CEMEREM, Marseille, France

³APHM, La Timone Hospital, Department of Epileptology and Clinical Neurophysiology, Marseille, France

⁴Aix-Marseille Univ, INS, INSERM UMR 1106, Marseille, France

Correspondence

Roy A. M. Haast, Aix-Marseille Université, Faculté de Médecine, CRMBM, 27 Boulevard Jean Moulin, 13385 Marseille Cedex 05, France.

Email: roy.haast@univ-amu.fr

Funding information

A*MIDEX, Grant/Award Numbers: AMX-19IET-004, 7TEAMS-Chair; Agence Nationale de la Recherche, Grant/Award Number: ANR-17-RHUS-0004; H2020 Marie Skłodowska-Curie Actions, Grant/Award Number: 101061988; Horizon 2020 Framework Programme, Grant/Award Numbers: 785907, 945539

Abstract

Focal epilepsy is characterized by repeated spontaneous seizures that originate from cortical epileptogenic zone networks (EZN). Analysis of intracerebral recordings showed that subcortical structures, and in particular the thalamus, play an important role in seizure dynamics as well, supporting their structural alterations reported in the neuroimaging literature. Nonetheless, between-patient differences in EZN localization (e.g., temporal vs. non-temporal lobe epilepsy) as well as extension (i.e., number of epileptogenic regions) might impact the magnitude as well as spatial distribution of subcortical structural changes. Here we used 7 Tesla MRI T_1 data to provide an unprecedented description of subcortical morphological (volume, tissue deformation, and shape) and longitudinal relaxation (T_1) changes in focal epilepsy patients and evaluate the impact of the EZN and other patient-specific clinical features. Our results showed variable levels of atrophy across thalamic nuclei that appeared most prominent in the temporal lobe epilepsy group and the side ipsilateral to the EZN, while shortening of T_1 was especially observed for the lateral thalamus. Multivariate analyses across thalamic nuclei and basal ganglia showed that volume acted as the dominant discriminator between patients and controls, while (posterolateral) thalamic T_1 measures looked promising to further differentiate patients based on EZN localization. In particular, the observed differences in T_1 changes between thalamic nuclei indicated differential involvement based on EZN localization. Finally, EZN extension was found to best explain the observed variability between patients. To conclude, this work revealed multi-scale subcortical alterations in focal epilepsy as well as their dependence on several clinical characteristics.

KEYWORDS

focal epilepsy, subcortical gray matter, multivariate analysis, T_1 , volume, shape, deformation

Roy A. M. Haast and Benoit Testud contributed equally to this work.

This is an open access article under the terms of the [Creative Commons Attribution-NonCommercial](https://creativecommons.org/licenses/by-nc/4.0/) License, which permits use, distribution and reproduction in any medium, provided the original work is properly cited and is not used for commercial purposes.

© 2023 The Authors. *Human Brain Mapping* published by Wiley Periodicals LLC.

1 | INTRODUCTION

Focal epilepsy is a chronic neurological disorder that is characterized by repeated spontaneous seizures caused by abnormal neuronal rhythms. These seizures typically start in one or several specific regions of the brain (i.e., epileptogenic zone, or EZ) and propagate to other regions or the whole brain. The EZ is part of a hierarchical network organization with subnetworks involved in the generation (i.e., epileptogenic zone network, EZN) and propagation (i.e., propagation network, PN) of epileptic activities across the brain (Bartolomei et al., 2017). Brain abnormalities might extend well beyond the EZ, involving regions that correlate with cognitive impairment but are only affected by seizure propagation or even spared from ictal discharges (i.e., non-involved networks). In approximately 30% of patients, epileptic seizures cannot be controlled by medication (Fattorusso et al., 2021; Kwan et al., 2010), thereby significantly hampering the patient's quality of life (Loring et al., 2004).

Network approaches—based on the mapping of inter-regional connectivity or covariance—showed that focal epilepsy indeed affects the whole-brain and that focal structural and functional changes within the EZ appear to act more as a set of nodes in a larger network of affected regions (Larivière et al., 2021; Rodriguez-Cruces et al., 2022). For example, changes in cortical morphometry and connectivity have been consistently observed across the cortical mantle (Drenthen et al., 2018; Larivière et al., 2020; Larivière et al., 2022; Whelan et al., 2018; Wirsich et al., 2016). Direct longitudinal relaxation time (T_1) mapping showed a prolongation of T_1 relaxation times in temporopolar, orbitofrontal and para-hippocampal regions indicating alterations at the microstructural level as well (Bernhardt et al., 2018).

Increasing evidence points to a crucial role for subcortical structures in facilitating and/or propagating epileptic activity (Pizzo et al., 2021) as integrative hubs for brain connectivity (Bell & Shine, 2016). In particular the thalamus, with its complex organization and nuclei, is a key gateway for cortico-subcortical interactions facilitating precise motor-sensory to broad cognitive functioning (Sherman, 2016; Shine, 2021). Not surprisingly, accumulating evidence using stereoelectroencephalography (SEEG; Guye et al., 2006; Pizzo et al., 2021; Rosenberg et al., 2006) and MRI (Bernhardt et al., 2012; Guye et al., 2006; Keller et al., 2014) reveal a prominent involvement of the thalamus in temporal lobe epilepsy (TLE). It has been demonstrated that previously observed cortical alterations in T_1 extend into the thalamic region as well, positioning thalamic T_1 as a promising metric to differentiate patients from controls (Tang et al., 2022) and complementing earlier observations of altered thalamic morphology (Keller et al., 2014; Whelan et al., 2018). Nonetheless, most of the published works has focused on the thalamus as a whole, a single metric, and/or a single type of focal epilepsy (mainly TLE). In addition, much of the current knowledge is derived from 3 Tesla (3T) MRI data which are suboptimal for identification of individual thalamic nuclei, as well as for detection of subtle differences across patients. Here, 7T MRI and its superior sensitivity is suitable alternative to probe the brain's subcortical gray matter at a much finer

scale and with superior tissue contrast in the context of both health and disease (Duyn, 2018; Marques et al., 2010; Opheim et al., 2020; Pohmann et al., 2016; Tractnig et al., 2018). Compared to 3T MRI, its increased signal-to-noise ratio provides unique opportunities for sub-millimeter quantification of changes specific to certain thalamic nuclei and regions which are difficult to identify at lower field strengths, such as the claustrum (Marques et al., 2010; Pohmann et al., 2016).

Thus, so far it has remained elusive how each of the previous, separate subcortical observations scale among each other based on (i) metric type (e.g., morphometry vs. T_1), (ii) thalamic nuclei and basal ganglia, and/or depend on (iii) the type of focal epilepsy (e.g., TLE vs. non-TLE) or (iv) clinical features (e.g., number of epileptogenic regions, seizure frequency, left vs. right seizure onset). By leveraging 7T MRI anatomical data, this study aims to fill this knowledge gap by using a multi-scale exploration of thalamic (nuclei) and basal ganglia alterations based on morphological (volume, deformation, and shape) and T_1 relaxation time parameters in a heterogeneous patient population consisting of TLE and non-TLE patients. Then, driven by the patient heterogeneity, we will employ a multivariate data-driven approach to highlight patterns within the subcortical MRI phenotype (i.e., combining all MRI features) that relate to differences in EZN and other clinical features.

2 | MATERIALS AND METHODS

2.1 | Study cohort

We retrospectively included all consecutive patients with drug-resistant focal epilepsy who underwent the presurgical evaluation at our center with available 7T brain MRI and SEEG recordings between June 2017 and October 2020. The SEEG recordings were performed in all patients as part of a routine clinical care according to the French guidelines (Isnard et al., 2018). The 7T MRI scans were acquired in the framework of two prospective studies recruiting patients undergoing presurgical evaluation for drug-resistant focal epilepsy: the EPINOV trial (NCT03643016) and the local EPI study. Both studies were approved by the local ethics committee, and all participants gave written consent. From the initial 52, five patients were excluded for sub-optimal quality of MRI data and two patients were excluded because SEEG was performed before the MRI. A last patient was excluded because of a large cerebral pial angioma that altered the anatomy and prevented adequate brain segmentation. Finally, data from 44 patients were used for further analyses. Patients were classified into five groups according to the EZN anatomo-functional organization as defined by visual and quantitative SEEG data analyses (Bartolomei et al., 2008) by expert neurologists (authors F.B. and J.M.): (i) temporal plus, with EZN either limited to the temporal regions or with maximal epileptogenicity within the temporal lobe but EZN extension to some extratemporal regions (e.g., temporo-insular, temporo-frontal, temporo-occipital, $N = 25$); (ii) prefrontal, with EZN involving prefrontal regions ($N = 8$); (iii) posterior, with EZN involving parietal and/or occipital regions ($N = 5$); (iv) insulo-opercular, with EZN involving the

insula and/or opercular cortex ($N = 3$); and (v) central-premotor, with EZN involving the primary motor and/or premotor cortex ($N = 3$). A second grouping-level was added by separating between temporal (i.e., temporal plus group patients, “TLE,” $N = 25$) and non-temporal patients (all other groups, “NTLE,” $N = 19$) together to gain statistical power. Finally, we recruited 33 age- and sex-matched healthy controls for comparison.

2.2 | Image acquisition

All data were acquired on a Siemens Magnetom 7T MRI system (Siemens Healthineers, Erlangen, Germany) equipped with a 32-channel head coil (Nova Medical, Inc., Wilmington, MA). Whole brain B_1^+ and T_1 maps were acquired using a spin-echo-based, assessing the ratio of consecutive spin and stimulated echoes and 3D Magnetization Prepared with 2 Rapid Acquisition Gradient Echoes (MP2RAGE) sequence, respectively (Marques et al., 2010). The MP2RAGE sequence produces a T_1 -weighted (T_1w) image with a spatially normalized contrast and minimal receive bias. Acquisition parameters were: $TR_{mpr}/TR/TE/TI_1/TI_2 = 5000/7.4/3.13/2750$ ms, $\alpha_1/\alpha_2 = 6^\circ/5^\circ$, FOV = 240 mm (matrix size: 402×402), 256 partitions, a parallel imaging acceleration factor of 3 (2D GRAPPA), and Partial Fourier factors of 6/8 in both phase- and partition-encoding directions. This resulted in a nominal isotropic voxel size = 0.6 mm and a total acquisition time of 10.12 min.

2.3 | Image preprocessing

The MP2RAGE data were used to segment thalamic nuclei and other basal ganglia for extracting morphometric and T_1 features. MP2RAGE anatomical data preprocessing included (i) correction for gradient non-linearities using the “*gradunwarp*” tool provided by the Human Connectome Project (HCP, <https://github.com/Washington-University/gradunwarp>); (ii) post hoc T_1 correction for residual B_1^+ inhomogeneities; (iii) a skull stripping workflow optimized for MP2RAGE data using “PreSurfer” and (iv) cortical surface reconstruction and parcellation using FreeSurfer (v7.1.1). The MP2RAGE data were corrected for B_1^+ inhomogeneities resulting in a “corrected” T_1w (i.e., UNI) and quantitative T_1 map, synthesized using a lookup table specific for the current sequence setup (<https://github.com/JosePMarques/MP2RAGE-related-scripts>; Marques & Gruetter, 2013). Non-brain tissue was then removed using the MP2RAGE’s second inversion and (corrected) UNI images using SPM12 functionalities wrapped within PreSurfer (<https://github.com/srikash/presurfer>; Kashyap, 2021; Kashyap et al., 2021). The skull stripped MP2RAGE T_1w images were used as input for the sub-millimeter processing workflow implemented in FreeSurfer (v7.1.1, <http://surfer.nmr.mgh.harvard.edu/>) image analysis suite to obtain brain tissue segmentations, estimated total intracranial volume (eTIV) and white matter and pial surface reconstructions (Fischl, 2012).

2.4 | Segmentation of thalamic nuclei and basal ganglia

2.4.1 | 7TAMIBrain

An improved version of the recently published 7TAMIBrain pipeline by Brun et al. was employed here for subcortical segmentation (Brun et al., 2022), making use of 60 atlases constructed from the 7TAMI-Brain dataset (Girard et al., 2021). This multi atlas label fusion (MALF; Wang et al., 2013) approach renders the segmentation results more robust and accurate, especially in cohorts with (potential) variable anatomies. The most important steps are highlighted below but see the [Supplementary Methods](#) for more details.

For each subject, its skull stripped T_1 map was first coregistered to each of the 60 atlases using the quick three stages registration procedure (i.e., rigid + affine + deformable SyN atlas-to-subject registrations), as implemented in ANTs “*antsRegistrationSyNQuick*” script (Avants et al., 2008; Avants et al., 2011). Fixed target (i.e., subject to segment) and moving (i.e., atlases) images were cropped (with matrix size = 192; Fattorusso et al., 2021) and centered on the DGN atlases pre-segmented via the single-atlas pipeline to optimize the computing time.

Second, the Joint Label Fusion algorithm and ANTs’ “*antsJointLabelFusion2*” script was used to merge the warped atlases into the individual subject’s space (Wang et al., 2013). Label fusion reduces the impact of potential biases from the image registration while providing a good spatial consistency for the label boundaries. By default, the Joint Fusion method is only performed in voxels for which the atlas’ labeling consensus is lower than 80%, otherwise Majority Voting is used to determine label assignment. For this work, Joint Fusion was used for any voxel for which full consensus was not reached across all atlases by setting this threshold at 100%. This reduces potential recurrent biases in the segmentation of epileptic subjects with large anatomical differences from the healthy controls of 7TAMIBrain dataset.

2.4.2 | THOMAS

To assess the impact of atlas choice on the thalamic results, thalamic nuclei were additionally segmented using THOMAS (Su et al., 2019). Since THOMAS is optimized to work with white matter-nulled (WMn) Magnetization Prepared with Rapid Acquisition Gradient Echoes (MPRAGE) images (i.e., enhanced thalamic-white matter contrast), MP2RAGE T_1 maps were first white matter-nulled using a recently proposed thresholding method based on the inversion recovery signal equation (Datta et al., 2021):

$$M_{synth} = M_0 \left(1 - 2e^{-\frac{t}{T_1}} \right). \quad (1)$$

Here, a T_1 threshold of 700 ms. was found to provide most reliable performance as assessed through visual inspection of segmentation results using varying thresholds. The WMn T_1 maps were then used as input for the joint-fusion THOMAS pipeline (https://github.com/thalamicseg/thomas_new).

2.5 | MRI feature extraction

Different MRI features were extracted from the MRI data using the thalamic (both atlases) and basal ganglia segmentations (7TAMIBrain atlas only).

2.5.1 | Volume-based features

For each ROI, total volume was computed (mm^3) while longitudinal relaxation time (T_1 , ms) were averaged across voxels. In addition, voxel-wise deformations were obtained by warping the 7TAMIBrain T_1 template to the subject's T_1 map. Here, a non-linear registration was performed using ANTs' deformable (diffeomorphic) registration (with shrink factors: $12 \times 6 \times 4 \times 2 \times 1$; smoothing factors: $6 \times 3 \times 2 \times 1 \times 0$ vox; max iterations: $100 \times 100 \times 70 \times 50 \times 10$; transformation model: SyN; similarity metric: cross-correlation; Avants et al., 2008). The resulting affine transformation matrix and non-linear transformation field were combined to obtain a single displacement field. Local change in tissue density was then estimated as the derivative of the displacement of a given voxel in each direction. The derivatives can be calculated as the determinant of the Jacobian matrix using ANTs' *ComputeJacobianDeterminant* function. The absolute value of the Jacobian determinant at voxel p gives us the factor by which the tissue expands or shrinks near p . By taking the logarithm of the determinant, no change is given by 0, tissue loss is given by a positive value, and tissue expansion is given by a negative value. Average deformation-based morphometry (DBM) values were obtained by averaging across all voxels within each ROI.

2.5.2 | Surface-based features

To assess changes in shape, surface-based metrics were extracted following the procedure described previously and using openly available image processing scripts (<https://github.com/khanlab/surfmorph>; Khan et al., 2019). The subject's T_1w image and labels were first aligned along the AC-PC plane, following the HCP procedure, to enable left-right flipping to combine analyses of the left and right hemisphere labels. Fuzzy labels for each of the subject's labels (ROIs) were then obtained by smoothing the binary ROI label with a $1 \times 1 \times 1$ mm kernel size. The fuzzy (i.e., smoothed) labels for each of the ROIs, for each subject, were transformed to MNI space using linear transformations based on the subject's MP2RAGE T_1w to MNI volume transformation. These linearly aligned labels were used to generate unbiased averages for surface generation by iterating through steps of (i) template generation by averaging across subjects, and (ii) registration of each segmentation image to this template using LDDMM registration. The resulting fuzzy segmentation was then used to generate the ROI's template surface through a 50% probability iso-surface. The 3D volume of the ROI's template was then fit to each subject's segmentation using LDDMM, with affine initialization to provide vertex-wise correspondence between all surfaces of that specific

ROI. The template surface was then propagated to each subject's ROI, to provide surfaces with common indices for projecting vertex displacement values and extraction of additional shape features. As such, vertex area and surface curvature were extracted using the "surface-vertex-areas" and "surface-curvature" Connectome Workbench (v1.5.0) command line functions, respectively (Marcus et al., 2011). Please, see Figure S1 for a schematic of this procedure.

Please note that single surfaces were constructed for the thalamus (i.e., by grouping thalamic nuclei) and striatum (i.e., caudate nucleus, nucleus accumbens, and putamen). However, nuclei-specific averages were calculated through thalamic and striatal surface atlases. To construct thalamic and striatal surface-based nuclei atlases, subject-specific volume labels were propagated toward the subject's surface models along the closest vertex normal, after which Majority Voting (i.e., across all subjects) was used to assign a label to each vertex. ROI-wise displacement, area and curvature were then reduced to a single shape component through principal component analyses.

2.6 | Statistical analysis

Prior to statistical analyses, ROI-results were corrected for confounding, linear effects of age, head size (both continuous), and sex (male vs. female) and hemisphere (left vs. right) using the *confounds* (v.0.1.1) Python package (Raamana, 2020). Contributions of confounding variables to the given feature were determined using a linear regression model based on data obtained in control subjects only. Control and patient feature data were then "residualized" by subtracting the contributions from the confound variables and z-scored using the controls' mean and standard deviation. An overview of the impact of each of these confounding factors on the different metrics can be found in Figure S2. Eventually, a data matrix of $N_{\text{subjects}} \times [N_{\text{feature type}} \times N_{\text{ROIs}} \times N_{\text{sides}}]$ was derived that was used as input for the following statistical analyses.

2.6.1 | Feature-wise comparison

Assessment of statistical differences of MRI features between subject groups was performed using (multivariate) analyses of variance (ANOVA). Besides correcting for age, head size, sex and hemisphere (see paragraph on confounder correction), multivariate ANOVA (MANOVA) and/or Bonferroni multiple comparisons correction was used in case of across nuclei and/or pair-wise statistical comparisons, respectively. Moreover, for each feature, ipsilateral minus contralateral differences were computed to assess possible unilateral changes.

2.6.2 | Partial least squares analyses

Partial least squares (PLS) analyses were carried out to further explore the variability in MRI-based features between groups (i.e., mean-centered PLS) and with respect to the clinical features

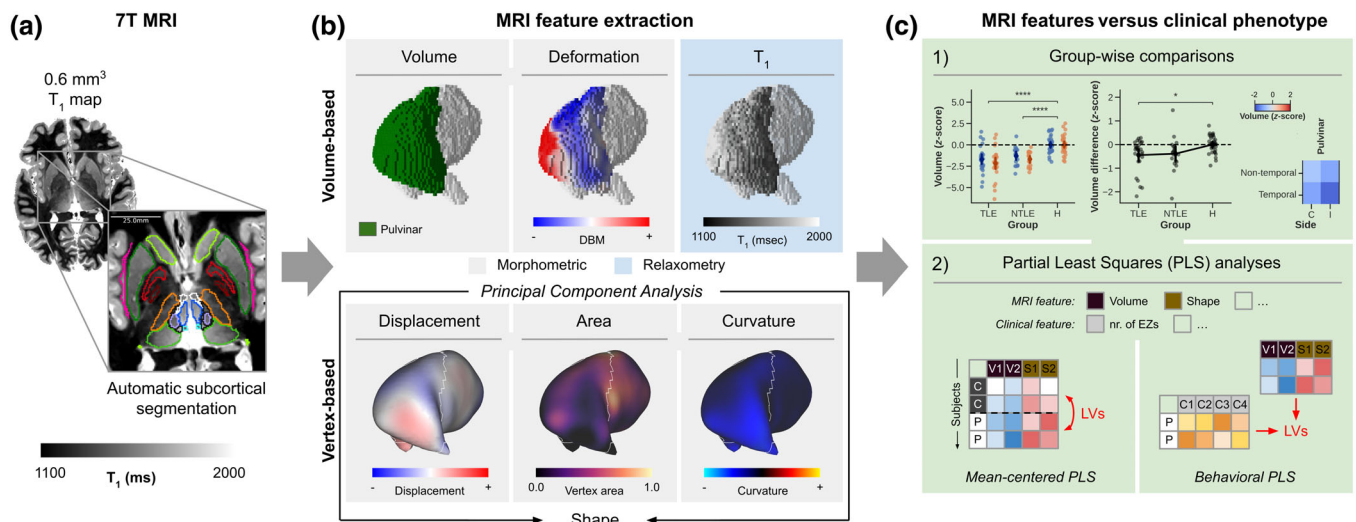


FIGURE 1 Schematic display of the analytical pipeline. (a) First, high resolution T₁ maps were used to segment the thalamus and other basal ganglia. (b) Several MRI features were then extracted, focusing on morphometry, and longitudinal relaxation time (T₁). Surface-based metrics related to shape (i.e., displacement, area, and curvature) were reduced to a single shape component. (c) Statistical analyses were performed for (1) group-wise comparisons as well as (2) identification of latent variables.

across patients (i.e., behavioral PLS) using the *PyPLS* Python package (<https://github.com/netneurolab/pypls>; Kirschner et al., 2020; McIntosh & Mišić, 2013). Compared to mass-univariate (Pearson or Spearman) correlation analyses, PLS works well with data characterized by multicollinearity, as is the case for the current collection of MRI features. Mean-centered PLS is a multivariate statistical approach that defines sets of variables in a matrix ($X_{n \times p}$) which maximally discriminate between subgroups within the matrix. Here, the n rows represent the individual subjects and p columns the MRI-based features. The resulting latent variable (LV) then constitutes a weighted combination of all MRI-based features that best differentiates groups (e.g., “TLE vs. NTLE vs. controls”). On the other hand, behavioral PLS identifies weighted patterns of variables across two given matrices ($X_{n \times p}$ and $Y_{n \times p}$) that maximally covary with each other. For example, when comparing patients' MRI-based features in matrix X and patients' clinical phenotype in matrix Y . Statistical evaluation of PLS results was performed using permutation tests ($N = 10,000$) to assess significance of overall patterns (i.e., LVs) and by bootstrap resampling ($N = 10,000$) to rank MRI and clinical features based on importance/reliability.

A graphical overview of the analytical pipeline is displayed in Figure 1. The directed acyclic graph in Figure S3 shows a detailed overview of the different (pre)processing steps.

3 | RESULTS

3.1 | Clinical features

Demographic characteristics and clinical data for all patients are shown in Table 1. The mean age at epilepsy onset was 12.6 (range

0.1–40) years, mean duration of epilepsy was 18.3 (range 2–47) years. Left and right seizure onset was observed in 23 (52%) and 21 (48%) cases, respectively, while on average 5.25 (range 1–14) regions were categorized as epileptogenic with a mean seizure frequency of 38.7 (range 2–300) per month. Anatomical MRI appeared normal in 25 (57%) and showed a structural abnormality in 19 (43%) of the cases based on 3T examinations. For one patient, the MRI showed a lesion at 7T while this was normal at 3T. Epilepsy etiology according to MRI and available histopathological findings included gliosis in seven, focal cortical dysplasia (FCD) type I/II/III in respectively five, nine and one patient(s), dysembryoplastic neuroepithelial tumor (DNET) in four; polymicrogyria (PMG) in two and periventricular nodular heterotopia (PNH) in two patients.

3.2 | MRI features

Figure 2 shows the full data matrix with rows representing subjects, grouped based on epilepsy type, and columns representing the individual MRI features organized per metric type (i.e., volume, deformation, shape, and T₁), brain structure (thalamic nuclei and other basal ganglia) and side with respect to seizure onset for patients (ipsilateral vs. contralateral), while based on hemisphere for control subjects. From this birds-eye view, both volume and T₁ show lower z-scores (i.e., brighter blue) for the patients compared to controls while the opposite pattern is true for deformation and shape (i.e., brighter red).

In the following sections will present these results in more detail focusing first on thalamic volume and T₁, after which these will be analyzed in conjunction with the remaining MRI features (deformation and shape), other basal ganglia data, as well as patient-specific clinical features using PLS analyses.

TABLE 1 Patient clinical demography.

Demographic			Epilepsy			Lesion info							
Patient	Age	Sex	Group	Epilepsy type	Side	Age at onset (years)	Disease duration (years)	Seizure frequency (per month)	Frequency of bilateral tonic-clonic seizures (per year)	Number of epileptogenic regions	3T MRI	7T MRI	Etiology/histological findings
sub-001	21	M	TLE	Temporal Plus	R	0.8	20	10	4	12	Lesion	Lesion	FCD2b
sub-002	22	F	TLE	Temporal Plus	R	13	9	150	0	8	Normal	Normal	Unknown/no abnormality
sub-003	25	F	TLE	Temporal Plus	L	10	15	2	0	1	Normal	Normal	FCD1
sub-004	40	M	NTLE	Prefrontal	R	16	24	90	0	8	Lesion	Lesion	Gliosis
sub-005	40	M	NTLE	Posterior	R	4	36	12	0	2	Normal	Normal	Unknown/no abnormality
sub-006	56	F	NTLE	Posterior	R	30	26	20	0	7	Lesion	Lesion	FCD2/NA
sub-007	44	M	NTLE	Insulo-opercular	L	13	31	2	0	3	Normal	Normal	Unknown/NA
sub-008	46	M	NTLE	Centra-Premotor	L	4	42	120	0	3	Lesion	Lesion	FCD2/NA
sub-009	48	F	TLE	Temporal Plus	R	40	9	30	0	3	Normal	Normal	FCD1
sub-010	33	F	TLE	Temporal Plus	R	24	9	4	0	3	Normal	Normal	FCD3a
sub-011	29	F	NTLE	Prefrontal	L	12	17	20	0	2	Lesion	Lesion	DNET
sub-012	27	F	NTLE	Centra-Premotor	L	4	23	90	0	4	Lesion	Lesion	FCD2b
sub-013	37	F	TLE	Temporal Plus	L	12	25	16	0	1	Lesion	Lesion	Ganglioglioma
sub-014	24	F	TLE	Temporal Plus	L	21	3	10	0	12	Normal	Normal	Unknown/NA
sub-015	28	F	NTLE	Prefrontal	L	0.1	28	90	0	2	Normal	Lesion	FCD2a
sub-016	36	M	NTLE	Posterior	R	3	33	300	0	3	Lesion	Lesion	FCD2b
sub-017	21	F	NTLE	Insulo-opercular	R	14	7	60	0	1	Lesion	Lesion	DNET
sub-018	31	F	NTLE	Prefrontal	L	8	22	30	0	2	Lesion	Lesion	FCD2b
sub-019	47	F	TLE	Temporal Plus	L	5	42	10	0	6	Normal	Normal	Unknown/NA
sub-020	29	M	TLE	Temporal Plus	L	3	26	120	0	2	Normal	Normal	Mild gliosis
sub-021	25	M	TLE	Temporal Plus	L	11	14	8	4	6	Normal	Normal	Unknown/NA
sub-022	23	M	TLE	Temporal Plus	L	12	11	8	0	4	Normal	Normal	FCD1
sub-023	26	M	NTLE	Prefrontal	L	17	10	50	0	6	Normal	Normal	FCD2a
sub-024	22	F	TLE	Temporal Plus	R	4	18	100	0	11	Normal	Normal	Unknown/NA
sub-025	15	M	TLE	Temporal Plus	L	2	13	5	0	7	Normal	Normal	FCD2a
sub-026	57	F	TLE	Temporal Plus	R	35	22	5	6	4	Lesion	Lesion	Gliosis

(Continues)

TABLE 1 (Continued)

Demographic			Epilepsy		Lesion info								
Patient	Age	Sex	Group	Epilepsy type	Side	Age at onset (years)	Disease duration (years)	Seizure frequency (per month)	Frequency of bilateral tonic-clonic seizures (per year)	Number of epileptogenic regions	3T MRI	7T MRI	Etiology/histological findings
sub-027	22	M	NTLE	Posterior	L	20	2	9	0	2	Lesion	Lesion	PMG
sub-028	17	M	NTLE	Insulo-opercular	L	7	10	12	1	5	Normal	Normal	Unknown/NA
sub-029	52	F	TLE	Temporal Plus	L	5	47	12	0	7	Lesion	Lesion	PMG, PNH
sub-030	30	M	TLE	Temporal Plus	L	3	26	15	6	5	Normal	Normal	Unknown/NA
sub-031	27	F	TLE	Temporal Plus	R	17	10	5	1	6	Normal	Normal	Unknown/NA
sub-032	42	F	TLE	Temporal Plus	L	28	14	15	6	4	Lesion	Lesion	Gliosis
sub-033	36	M	TLE	Temporal Plus	R	29	7	60	12	3	Normal	Normal	FCD1
sub-034	41	M	NTLE	Prefrontal	R	12	29	60	0	2	Normal	Normal	Unknown/NA
sub-035	18	F	TLE	Temporal Plus	R	13	5	15	6	6	Normal	Normal	Mild gliosis
sub-036	38	F	TLE	Temporal Plus	R	20	18	68	0	4	Lesion	Lesion	PNH, FCD1
sub-037	30	M	TLE	Temporal Plus	L	19	21	2	0	6	Normal	Normal	Unknown/NA
sub-038	20	M	NTLE	Prefrontal	R	7	13	15	0	11	Lesion	Lesion	Pediatric infiltrative glioma
sub-039	31	M	TLE	Temporal Plus	R	22	9	4	0	5	Normal	Normal	Mild gliosis
sub-040	21	M	TLE	Temporal Plus	L	12	9	2	0	3	Lesion	Lesion	Ganglioglioma
sub-041	16	M	NTLE	Posterior	R	10	6	10	12	14	Normal	Normal	Unknown/NA
sub-042	21	F	NTLE	Prefrontal	R	9	11	5	0	1	Normal	Normal	Mild gliosis
sub-043	16	M	TLE	Temporal Plus	R	1.5	14	30	0	13	Lesion	Lesion	DNET
sub-044	17	M	NTLE	Centra-Premotor	L	0.5	17	2	0	11	Lesion	Lesion	DNET

Abbreviations: DNET, dysembryoplastic neuroepithelial tumor; FCD, focal cortical dysplasia; L/R, left/right; M/F, male/female; NA, not applicable; NTL non-temporal lobe epilepsy; PMG, polymicrogyria; PNH, periventricular nodular heterotopia; TLE, temporal lobe epilepsy.

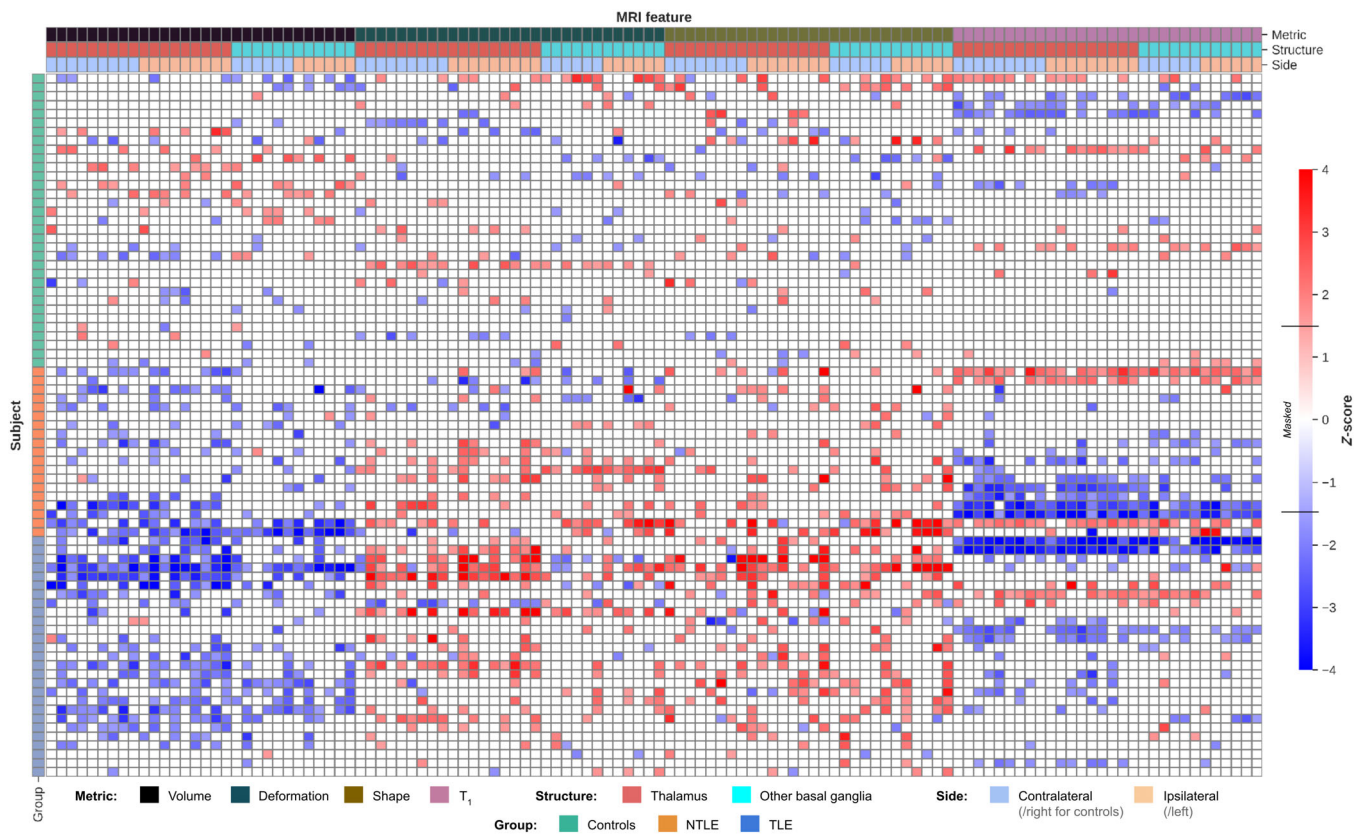


FIGURE 2 Z-scores heatmap. Individual MRI features are color-coded (thresholded at -1.5 and 1.5) as indicated by the horizontal bars on the top according to metric type (volume, deformation, shape, and T_1), brain structure (thalamus vs. other basal ganglia) and side with respect to seizure onset for patients (contra- vs. ipsilateral), while left versus right for control subjects. Vertical color bars on the left side indicate subject group.

3.2.1 | Volume

Previous work has shown thalamic volume reduction in TLE. To confirm these effects in the current study cohort, as well as to investigate potential TLE and NTLE and nuclei-specific differences, we compared thalamic changes at a global scale (i.e., whole thalamus) as well as at the single nucleus-level.

At the level of the whole thalamus (Figure 3a), ipsilateral and contralateral thalamic volumes were significantly different between groups ($F_{2,76} = 20.68$, $p < .001$). Both groups of patients had lower volumes compared to controls ($p < .001$). Thalamic volume was lower in the thalamus ipsilateral to the epileptogenic zone compared to controls in TLE ($p < .05$), but not in NTLE ($p = .06$). No significant differences were observed between TLE and NTLE.

Thalamic nuclei volumes (Figure 3b) were lower than controls in both focal epileptic groups ($F_{18,138} = 3.502$, $p < .001$; Wilk's $\Lambda = 0.471$, partial $\eta^2 = .31$). The strongest general group effect was observed in the mediodorsal nucleus ($F_{2,77} = 22.038$, $p < .001$) with differences originating from both TLE and NTLE (both $p < .001$) groups compared to controls. The weakest (and only not significant) group effect was observed for the anterior nucleus ($F_{2,77} = 2.956$, $p = .058$). Asterisks below nuclei labels indicate MANOVA (black), and pairwise comparison (orange for TLE and blue for NTLE, vs. controls) results. Multivariate analysis across

thalamic nuclei did not show systematic ipsi- versus contralateral volume differences between groups.

For brevity reasons, see the [Supplementary Results](#) (section “Deformation and shape”) for extension of these analyses to the other morphometric features.

3.2.2 | T_1 relaxometry

Thalamic T_1 relaxometry values (Figure 4a) were significantly modulated by group ($F_{2,76} = 3.80$, $p < .05$), with differences coming from the TLE patients compared to controls ($p < .05$).

As for volume, thalamic nuclei T_1 (Figure 4b) values were lower than controls in both focal epileptic groups ($F_{18,138} = 2.230$, $p < .01$; Wilk's $\Lambda = 0.600$, partial $\eta^2 = .24$). Here, the lateral group shows the strongest effect ($F_{2,77} = 3.228$, $p < .005$) with similar contributions from TLE ($p < .05$) and NTLE ($p < .05$) patients. As for volume, the weakest effect was seen for the anterior nucleus (N.S.). T_1 was not significantly different between the ipsi- and contralateral sides.

3.3 | MRI versus clinical features

In previous sections we reported on thalamic changes, focusing on the MRI features separately. Nonetheless, it remains unclear which

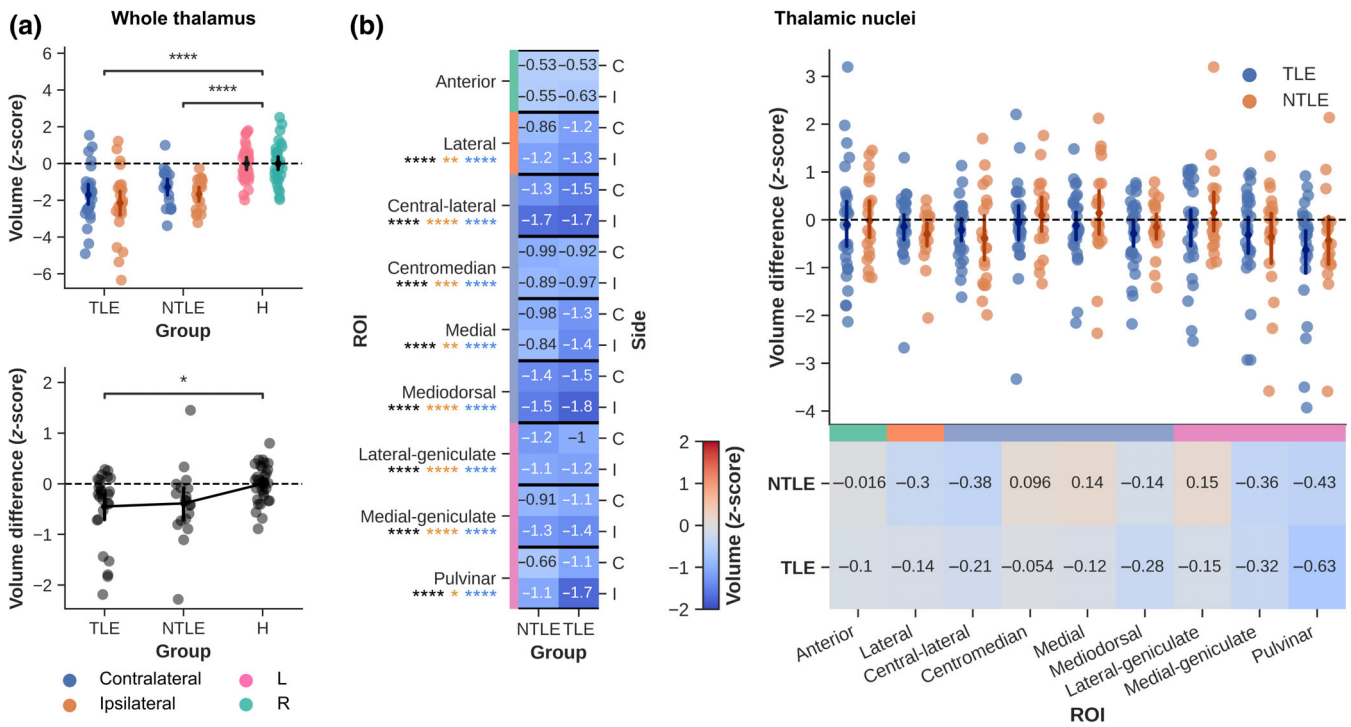


FIGURE 3 Volumetric results. (a) Whole thalamic volume (z-scored) was compared between groups (top panel) as well as between sides (i.e., ipsilateral-contralateral differences for patients, left-right for controls, bottom panel). (b) Similarly, average volumes of each thalamic nuclei (z-scored) are shown for both patient groups (columns) and side (rows, left heatmap). Asterisks below nuclei labels indicate MANOVA (black), and pair-wise comparison (orange for NTLE and blue for TLE, vs. controls) results. Strip plot and right heatmap in B illustrate the ipsilateral-contralateral T₁ differences for each patient (color-coded by group). Color-bars alongside nuclei labels indicate group assignment. C = contralateral; I = ipsilateral; **p* < .05; ***p* < .01; ****p* < .005; *****p* < .001; Bonferroni corrected in case of multiple comparisons.

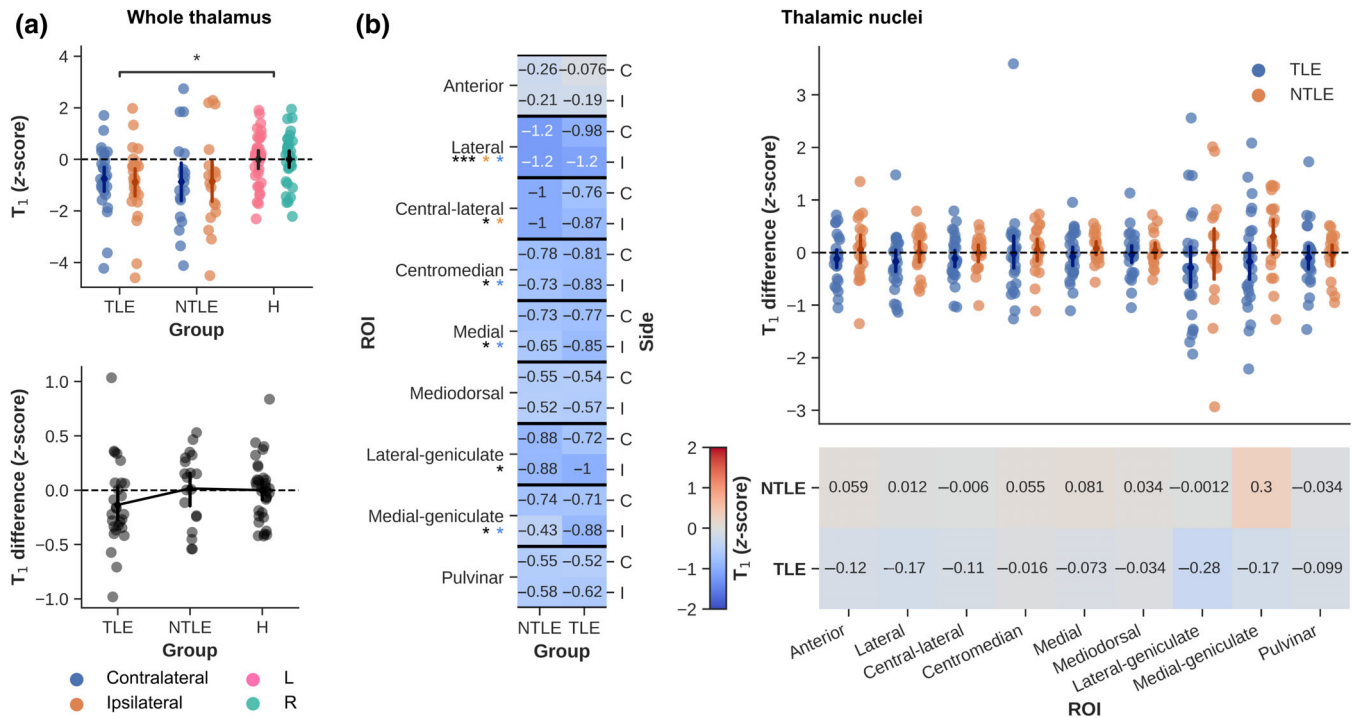


FIGURE 4 T₁ results. (a) Whole thalamic T₁ (z-scored) was compared between groups (top panel) as well as between sides (i.e., ipsilateral-contralateral differences for patients, left-right for controls, bottom panel). (b) Similarly, average T₁ of each thalamic nuclei (z-scored) are shown for both patient groups (columns) and side (rows, left heatmap). Asterisks below nuclei labels indicate MANOVA (black), and pairwise comparison (orange for NTLE and blue for TLE, vs. controls) results. Strip plot and right heatmap in B illustrate the ipsilateral-contralateral T₁ differences for each patient (color-coded by group). Color-bars alongside nuclei labels indicate group assignment. C = contralateral; I = ipsilateral; **p* < .05; ***p* < .01; ****p* < .005; *****p* < .001; Bonferroni corrected in case of multiple comparisons.

feature(s) provide(s) the most discriminatory power between groups and/or across patients when analyzed together as well as the added value of the other basal ganglia. As such, in the following we performed mean-centered and behavioral PLS analyses to rank MRI and clinical features in terms of importance/reliability, respectively.

3.3.1 | Mean-centered PLS

Mean-centered PLS allows to rank individual MRI features based on their contribution to LVs that significantly differentiate(s) between subject groups. Contrasting MRI features between NTLE, TLE and controls resulted in one significant LV (81.4% explained variance, $p_{\text{perm}} < .001$). Figure 5a shows the ranking and comparison of the MRI features (color-coded as in Figure 2) in terms of their absolute contribution to the LV as defined by their bootstrapped ratio (BSR) between the feature's loading and its 95% confidence interval. Metric, structure, and side-wise averages are shown using black diamonds ($\pm 95\%$ CI). Here, BSRs were significantly modulated by metric type ($F_{3,102} = 12.27$, $p < .001$) with higher BSRs observed for the volumetric features compared to deformation-, shape-, and T_1 -based features (all $p < .001$). Although different in magnitude, a clear spatial correlation between volume and shape features can be observed when projecting the BSR value onto their respective surface reconstructions, with higher BSR values toward the ipsilateral, posterior thalamus (Figure 5b).

A weaker, but nonetheless significant LV was detected when contrasting the five epilepsy types (62.3% explained variance, $p_{\text{perm}} < .05$, Figure 6). Again, BSRs varied as function of metric type ($F_{3,102} = 12.27$, $p < .001$), but structure as well ($F_{1,102} = 11.71$, $p < .005$). Here, highest BSRs were observed for the T_1 -based features ($p < .005$ compared to volume and $p < .001$ compared to shape). Moreover, changes in thalamic nuclei appear more strong contributors than changes in the other basal ganglia ($p < .005$). See Figure S3 for surface-wise projections.

3.3.2 | Behavioral PLS

Focusing on the patient data only, behavioral PLS provides a mean to evaluate patterns based on both MRI and clinical features, independent of epilepsy type. This revealed one significant LV (35.2% explained variance, $p_{\text{perm}} < .05$). Here BSRs were significantly modulated by metric type ($F_{3,102} = 13.91$, $p < .001$), structure ($F_{1,102} = 6.814$, $p < .05$) and side ($F_{1,102} = 7.680$, $p < .01$). Contributions predominantly came from T_1 ($p < .001$ compared to deformation-based features), thalamic ($p < .05$ compared to other basal ganglia) and contralateral ($p < .05$ compared to ipsilateral) features (Figure 7a). With regards to the clinical characteristics, strongest contributions were found for the number of epileptic zones, but also presence of MRI-detectable lesion(s), disease duration (years) and seizure frequency (all $p_{\text{boot}} < .05$, Figure 7b). Pink bars indicate associations that were significant at $p_{\text{boot}} < .05$. Surface projections reveal

that volume features contributing robustly to the LV were found predominantly within the thalamus, while T_1 features were found more widespread across the basal ganglia (Figure S4). Again, volume and shape show similar surface-wise projections.

Finally, the scatterplots in Figure 7c visualize the correlations between covarying MRI and clinical features (number of epileptic zones and visible lesion, yes/no). We choose to show the MRI features with the highest BSR for each metric type. Here, lateral thalamic volume was lower in patients characterized by an increased number of epileptic zones, $r(42) = -.35$, $p < .05$. A similar (but inverse) pattern is visible for the claustrum's shape, $r(42) = .37$, $p < .05$. T_1 in the lateral geniculate nucleus seem to be reduced in patients with a visible lesion compared to patients without a lesion ($p < .05$).

3.4 | Replicating using THOMAS

To assess the dependence of current results on the atlas choice, all analyses were repeated but using the THOMAS atlas for the thalamic segmentations. These can be found in the [Supplementary Results](#) (section "Replicating using THOMAS"). Briefly, analyses conducted using thalamic results using the THOMAS atlas showed the same direction of differences as with the 7TAMIBrain atlas. Nonetheless, while remaining below significance threshold using the 7TAMIBrain atlas, the impact of seizure onset side was stronger across the different metrics using THOMAS. For example, average ipsi- versus contralateral T_1 differed significantly between TLE and NTLE patients ($p < .05$).

4 | DISCUSSION

Our cohort of focal epilepsy patients showed unprecedentedly described structural abnormalities across the thalamus and basal ganglia. In general, the strongest impact was observed for TLE patients. The spatial pattern of these differences and the contribution of the different metrics varied depending on whether the patient data was contrasted against controls or among themselves.

4.1 | Thalamic structural alterations

Focal epilepsy patients showed significant reduction in thalamic volume, as well as increased—although characterized by smaller effect sizes—tissue deformation and shape values. These indicators of atrophy are in line with prior research in TLE (Bernhardt et al., 2012; Keller et al., 2014; Natsume et al., 2003) and as recently demonstrated on a larger scale using the multisite ENIGMA Epilepsy dataset (Whelan et al., 2018). Here, we confirm this phenomenon in our TLE and NTLE focal epilepsy cohort. This is not surprising given the widespread thalamo-cortical connectivity (Lambert et al., 2017) and its implications in seizure initiation, propagation, spread (Bertram et al., 2008; Guye et al., 2006; Pizzo et al., 2021) as well as focal to bilateral tonic-clonic seizures (Sinha

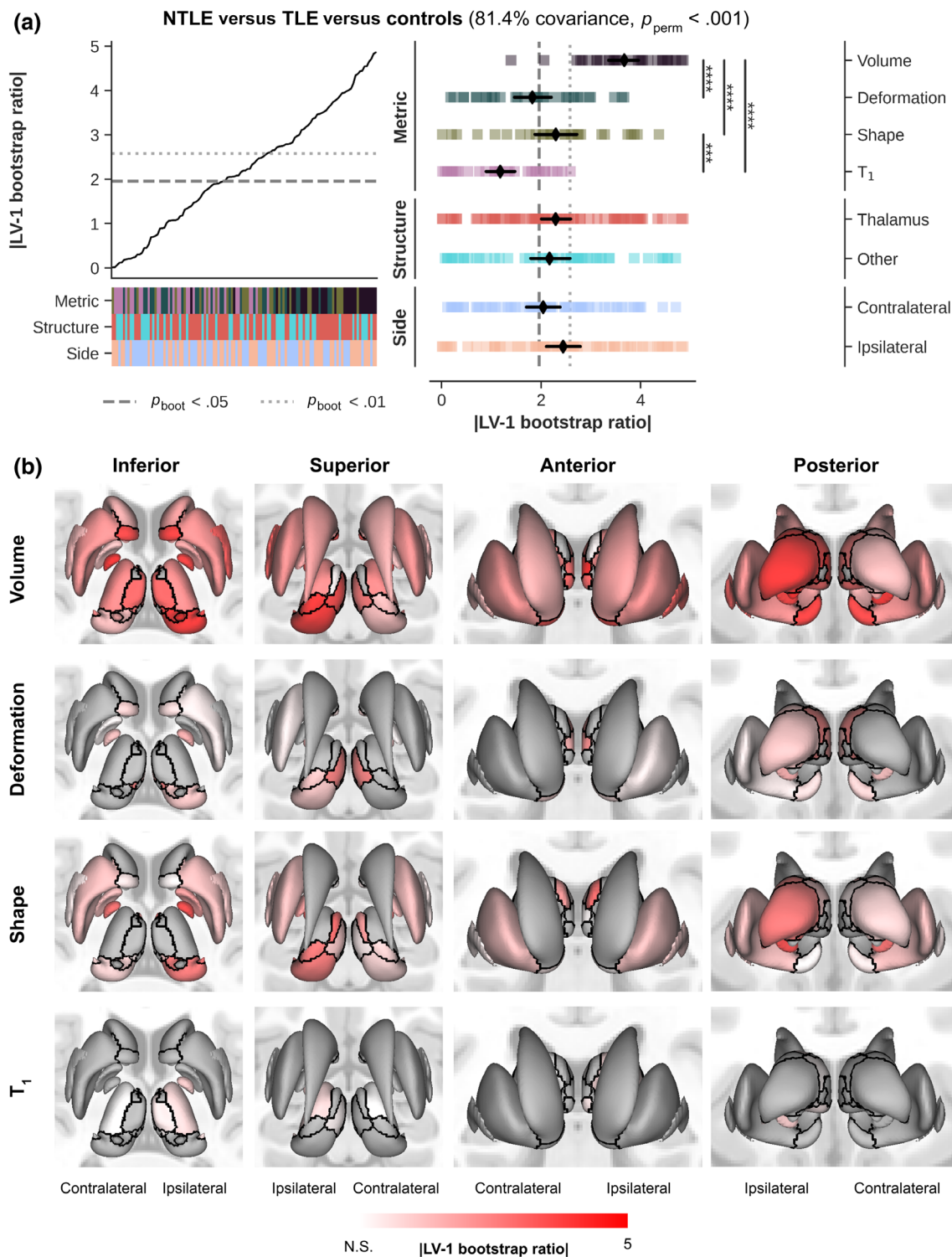


FIGURE 5 Mean-centered PLS results across patients and controls. (a) Line plot shows sorted bootstrapped ratios when contrasting NTLE, TLE, and controls. Heatmaps indicate feature properties (metric type, structure, and side, color-coded as in Figure 2). Strip plot shows the decomposition of features based on feature properties with black diamonds indicating average BSR ($\pm 95\%$ CI). $*p < .05$; $**p < .01$; $***p < .005$; $****p < .001$; Bonferroni corrected in case of multiple comparisons. (b) Projection of significant bootstrapped ratio values (color-coded), based on mean-centered partial-least squares analyses, onto the structures' surface reconstructions. Results are separated per MRI metric type (rows). Black solid lines indicate structure boundaries.

et al., 2021). Moreover, the ipsilateral predominance of global thalamic atrophy could intuitively be explained by the thalamo-cortical connectivity during seizures. This has been illustrated previously by

accurate prediction of seizure onset laterality in TLE patients based on individual thalamo-hippocampal functional connectivity scores (Barron et al., 2015).

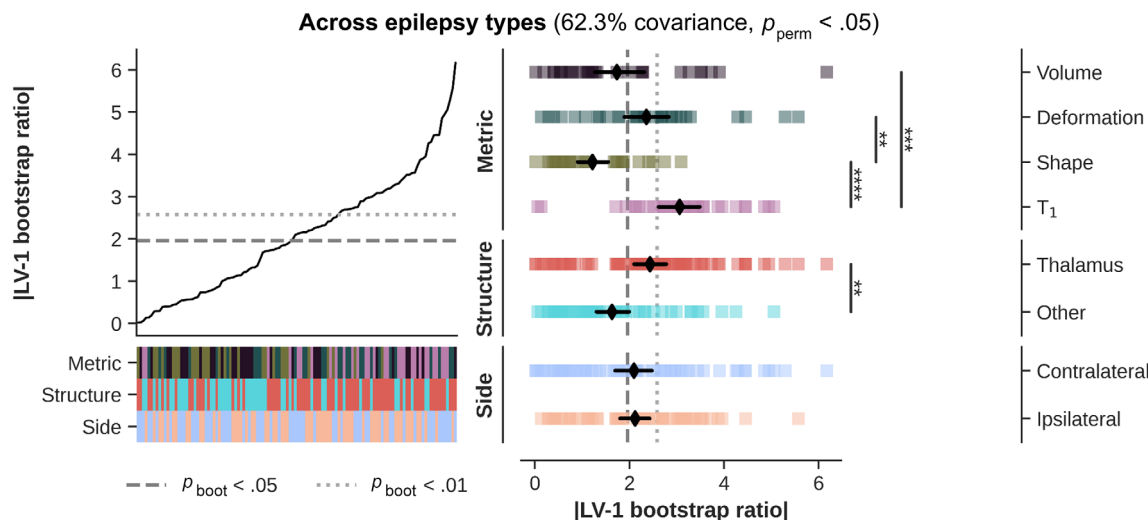


FIGURE 6 Mean-centered PLS results across patients. Line plot shows sorted bootstrapped ratios when contrasting epilepsy types (i.e., temporal plus, prefrontal, posterior, insulo-opercular, and central-premotor). Heatmaps indicate feature properties (metric type, structure, and side, color-coded as in Figure 2). Strip plot shows the decomposition of features based on feature properties with black diamonds indicating average BSR ($\pm 95\%$ CI). * $p < .05$; ** $p < .01$; *** $p < .005$; **** $p < .001$; Bonferroni corrected in case of multiple comparisons.

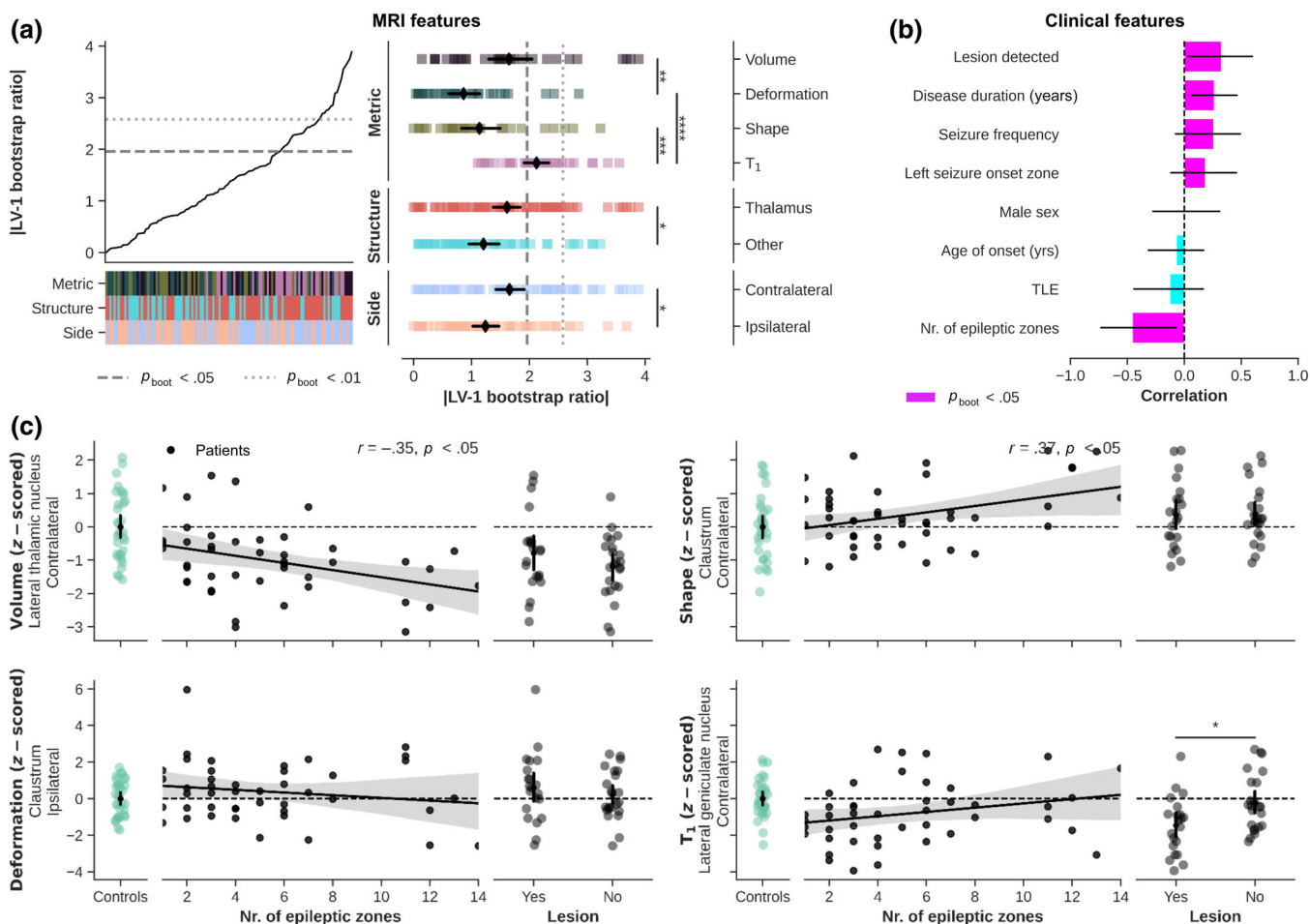


FIGURE 7 Behavioral PLS results. (a) Line plot shows sorted bootstrapped ratios with heatmaps indicating feature properties (metric type, structure, and side, color-coded as in Figure 2). Strip plot shows the decomposition of features based on feature properties with black diamonds indicating average BSR ($\pm 95\%$ CI). (b) Ranking of clinical features in terms of correlation with the LV. (c) Correlation between clinical features and MRI-based z-scores. * $p < .05$; ** $p < .01$; *** $p < .005$; **** $p < .001$; Bonferroni corrected in case of multiple comparisons.

Deformation and shape might provide complementary and spatial-specific insight into volume-based thalamic structural alterations, especially at the scale of individual thalamic nuclei. Indeed, the lack of significant effects for the medial nucleus for both deformation and shape are indicative of spatially homogeneous alterations leading to an overall decrease in volume. Conversely, differences in shape and deformity may reflect preferential changes in pulvinar subparts that sum up to atrophy based on volume alone. In addition, isolated changes in the deformation of the anterior nucleus of the thalamus without volume, T_1 , or shape changes may suggest structural remodeling. Please see Section 6.2 for a more in-depth discussion at the level of the individual nuclei.

Most interestingly, we report longitudinal relaxation data for the thalamus and other basal ganglia in both TLE and NTLE drug-resistant patients characterized by SEEG (i.e., Figure 2). In contrast to the data reported in the cortex (Bernhardt et al., 2018) and thalamus previously (Tang et al., 2022), we found a decrease in thalamic T_1 . It is known that T_1 shortens with increasing myelin and iron (i.e., ferritin) concentrations (Stüber et al., 2014). Therefore, the observed decrease in T_1 can be attributed to higher levels of myelin and/or iron in patients compared to controls. In particular the latter is a hallmark of several neurological and neurodegenerative diseases (Ward et al., 2014). In epilepsy, using pilocarpine-treated rats to induce a status epilepticus, iron (and calcium) deposits were selectively observed across the thalamus (Aggarwal et al., 2018). Potential mechanisms leading to iron accumulation include increased blood–brain barrier (BBB) permeability, inflammation, iron redistribution within the brain, and changes in iron homeostasis (Ward et al., 2014). It remains unclear, however, if these abnormalities are mainly caused by seizures, or by the evolution of the disease and neurodegenerative processes. Leek et al. (2021) showed that volumetric abnormalities of structures known to be important for the generation and maintenance of focal seizures are established at the time of epilepsy diagnosis and are not necessarily a result of the chronicity of the disorder (Leek et al., 2021). On the other hand, longitudinal tracking of cortical thickness in TLE patients showed progressive thinning with longer disease duration, particularly in regions structurally connected with the ipsilateral hippocampus (Galovic et al., 2019).

Furthermore, differences between cortical and thalamus tissue and their increase (Bernhardt et al., 2018) versus decrease in T_1 , respectively, might be explained based on their tissue's organization including their connectivity. Cortical cyto- and myeloarchitecture is organized in a laminar fashion along a sheet-like structure with cortical myelination gradually decreasing toward the pial surface and layer-specific feed-forward and feedback projections (Nieuwenhuys, 2013). This laminar organizational principle is not in place for thalamic gray matter with nuclei-specific (sub)cortical projections (Morel et al., 1997). This imposes a dense network of innervating fiber bundles with high levels of crossing fibers (Behrens et al., 2003; Clascá et al., 2012). Given the important role of the thalamus in seizure organization and therefore widespread participation during seizures, changes in thalamic T_1 might be dominated by pathophysiological processes (e.g., BBB dysfunctioning; Rüber et al., 2018) that cause iron to

accumulate (Pizzo et al., 2021; Ward et al., 2014). In contrast, demyelination as also observed in postsurgical tissue derived from cortical dysplasia might be the predominant driver of the increase in cortical T_1 (de Curtis et al., 2021). Also, while atrophy has been observed across both cortical and subcortical areas, differences in the microstructural environment (e.g., macromolecular composition) might render the impact of neuronal loss on T_1 relaxation differently (Beaulieu, 2002; Mezer et al., 2013). Nonetheless, based on T_1 relaxation time alone, it remains difficult to explain the histological and molecular translation of the observed changes. Multivariate analyses with other quantitative metrics, like the tissue's transverse relaxation time (T_2^*), susceptibility value (QSM) and diffusion properties (e.g., fractional anisotropy and mean diffusivity) are necessary to better explain this observed decrease in T_1 . This has proven to be beneficial at the cortical level with better discrimination of normal and abnormal neuron density in neocortical gray matter when T_1 is combined with FA (Goubran et al., 2015), leading to better separation between left and right TLE (Khan et al., 2014).

4.2 | Multi-scale structural alterations

The thalamus as a whole and by itself provides relevant information to better understand the disease processes in focal epilepsy. However, the human thalamus hosts several nuclei with varying cytoarchitectonic features and projections innervating distinct (sub)cortical regions (Clascá et al., 2012; Jones, 2009). Therefore, thalamic nuclei might be differentially affected depending on epilepsy type (i.e., TLE vs. NTLE), EZN characteristics and other clinical features. Moreover, thalamic connectivity with basal ganglia warrant investigation of covarying patterns among subcortical structures (DeLong & Wichmann, 2007; Kai et al., 2022; Lenglet et al., 2012). To do so, we performed multivariate mapping of MRI-based subcortical features and patient characteristics (i.e., epilepsy type or clinical features) using mean-centered and behavioral PLS (Kirschner et al., 2020; McIntosh & Mišić, 2013), to isolate latent clinical-anatomical dimensions of focal epilepsy. Understanding the heterogeneity of clinical and anatomical manifestations of focal epilepsy remains a major challenge (Whelan et al., 2018). A closer inspection and comparison of the primary LVs derived from PLS analyses using the data presented here revealed several interesting findings. First, while volume-based measures appeared to be most discriminative when control data were included, T_1 measurements gain importance with respect to other metric types when discriminating across patients only. This was evident based on the MRI features only (i.e., mean-centered PLS), as well as when combined with the clinical features (behavioral PLS). Second, the spatial patterns of the LVs appear to be characterized by different topological modes with robust features either (i) confined to a set of thalamic nuclei or (ii) spread across the entire subcortex. When focusing on the thalamus again, morphometric abnormalities within the posteromedial thalamus, including the pulvinar and mediodorsal nucleus, acted as dominant discriminators between patients and controls. On the other hand, epilepsy types were best separated by their T_1 within the

posterolateral portion of the thalamus, in particular. Together, these patterns follow the same trend as the group-level analyses and suggest that predisposition of thalamic nuclei to alterations (Aggarwal et al., 2018) may depend on the property being evaluated but also on clinical characteristics, such as the location and/or number of epileptogenic zones. The medial pulvinar has been implicated in focal epilepsy based on frequently observed ictal activity changes during temporal lobe seizures (Guye et al., 2006; Rosenberg et al., 2006) and its atrophy (Keller et al., 2014) has been proposed as potential target for therapeutic deep brain stimulation (DBS) in drug-resistant epilepsies (Filipescu et al., 2019). Similarly, given its connectivity with the amygdala and temporal cortex (Behrens et al., 2003), the mediodorsal nucleus has been studied in the context of (medial) temporal lobe epilepsy. For example, rats experiencing status epilepticus and then developing epilepsy had a decrease in volume of the mediodorsal thalamic region related to histological indicators of neuronal loss (Bertram et al., 2001). Extending these findings to humans, mediodorsal and posterior thalamic gray matter density was reduced in TLE patients (Barron et al., 2012) and in patients with persistent seizures compared to patients without seizures after surgery (Keller et al., 2015). On the other hand, spatial specificity of T_1 decreases toward the lateral thalamus in focal epilepsy (as well as across epilepsy types) could be explained by the interaction between activity-regulated myelination (Gibson et al., 2014) and seizure pathophysiology. Increased seizure network myelination after epilepsy onset has recently been demonstrated in rat models of absence seizures and generalized epilepsy (Knowles et al., 2022). This, together with the strong connectivity of the lateral thalamus to somatosensory, posterior and parietal areas, organized along an anterior–posterior axis, might explain the consistent decrease in T_1 for the lateral thalamic nuclei in our patient cohort (Behrens et al., 2003). The anterior nucleus volume and T_1 appeared relatively unaffected. This is surprising given the frequent involvement of the limbic system in the TLE group. Potential explanations could be its small size, shape variability (as also shown in this work; Hughes et al., 2012), and its close vicinity to white matter (i.e., internal medullary lamina) which can influence segmentation accuracy. Furthermore, anterior nucleus atrophy has been reported to be particularly associated with hippocampal sclerosis, which was not reported in our cohort (Chan et al., 1997).

However, in line with earlier work using structural covariance networks in TLE and idiopathic generalized epilepsy (Whelan et al., 2018), our LVs show that volume-based patterns extend beyond the thalamic borders and involve basal ganglia such as internal globus pallidus and striatum as well. This pattern might represent the same shared patterns of structural abnormalities across different epilepsies as suggested by Whelan et al. (2018), despite the heterogeneity of epilepsy and seizure types. Our results complement other recent studies of multivariate analyses in focal epilepsy. For example, Lee et al. (2022) identified several MRI-based components spanning cortical and white matter tissue that described interindividual variability in TLE. Within a framework to predict treatment response or surgery outcome, these outperformed classifiers that did not operate on latent factor information. Another multivariate approach emphasized a close

coupling of cognitive dysfunction and large-scale network anomalies in TLE (Rodríguez-Cruces et al., 2020). Here we show that subcortical volume measures allow discrimination between patients and controls, while T_1 measures look promising to further differentiate patients based on epilepsy type. Altogether, these multivariate results demonstrate the brain-phenotypic complexity of focal epilepsy at the whole-brain scale with the extent, interplay and type of changes depending on brain compartment as well as clinical phenotype.

4.3 | Methodological considerations and study limitations

Although the consistency across thalamic segmentation protocols corroborates the robustness of our results, they might not be generalizable to external datasets and those acquired at lower field strengths, in particular.

T_1 is dependent on magnetic field strength with the level of dependency varying based on tissue characteristics (i.e., low vs. high molecular mobility; Rooney et al., 2007). It has been shown that 7T allows detection of epileptogenic lesions not visible at 3T (Opheim et al., 2020). Therefore, based on typical acquisitions performed at 3T and 7T, differences in the signal- and contrast-to-noise ratios of T_1 data will impact sensitivity to segment individual nuclei as well as the power to detect patient-control morphometric and T_1 differences at lower field strengths (Le Ster et al., 2022; Pohmann et al., 2016). Precise delineation and quantification of thalamic nuclei and basal ganglia have become feasible with the advent of 7T MRI and the possibility to map T_1 both at a submillimeter resolution and (relatively) fast using the MP2RAGE sequence (Marques et al., 2010). As a result, multiple protocols have been proposed, including the one developed in-house (Brun et al., 2022), to segment thalamic nuclei and basal ganglia from such data (Datta et al., 2021; Su et al., 2019). When we compared results from our in-house 7TAMIBrain atlas method with those from another popular approach (THOMAS), thalamic volumetric measurements appear relatively similar despite differences in segmentation algorithm and nuclei definitions. In addition, brain tissue segmentations based on (quantitative) MRI data like transmit field (B_1^+)-corrected MP2RAGE maps are known to be more robust and accurate than those based on uncorrected images affected by residual B_1^+ biases (Haast et al., 2018; Haast et al., 2021; Marques & Gruetter, 2013). In parallel, current results provide a proof-of-concept to assess morphometric and T_1 properties of the claustrum—a deep brain structure characterized by challenging anatomy with its thin sheet of neurons, enclosed by white matter and situated between the insula and the putamen (Mathur, 2014)—in a clinical population.

Our cohort is limited in the number of patients diagnosed with non-temporal epilepsies. Consequently, we have pooled all NTLE patients into a single patient group, with the risk of losing sensitivity during group-level comparisons. Moreover, the statistical significance of the PLS LVs were evaluated within a descriptive framework to detect above-chance associations in the current dataset. As such, we did not test whether such associations generalize to new data. For

example, our cohort consists of rather challenging patients that required SEEG and replication using a separate cohort with a different number of patients per epilepsy type might rank MRI features differently and lead to different conclusions. Evaluation of out-of-sample correlation and predictive performance using an independent and larger study cohort is needed. It is therefore our hope that in the future a similar action will be undertaken to establish a multisite 7T epilepsy data as achieved by the ENIGMA Epilepsy study group (Sisodiya et al., 2022). As a first step, recent efforts by the 7T Epilepsy Task Force led to practical recommendations on targeted use of 7T MRI in the clinical management of patients with epilepsy (Opheim et al., 2020). Such datasets will help mitigate problems related to limited sample sizes as well as means to investigate potential methodological biases.

5 | CONCLUSION AND FUTURE DIRECTIONS

This work reveals multi-scale—based on multiple parameters across different structures—subcortical alterations in focal epilepsy patients using 7T MRI data. It shows that the relative importance for different MRI features across subcortical structures depend on whether the goal is to isolate patients from controls or to differentiate between epilepsy types. Moreover, these results provide a comprehensive representation of the subcortical phenotype of focal epilepsy and its correlation with clinical parameters. In future work, integration of (i) other quantitative MRI, as well as (ii) electrophysiological data might allow us to better understand its direct relation to the structures' microstructural and epileptogenic properties, respectively. Moreover, extending this framework to the cortex provides opportunities to investigate the impact of subcortical alterations on the brain's system-wide functioning. Finally, since deep brain stimulation is largely based on empirical protocols, comprehensive mapping of subcortical changes and relationship with disease heterogeneity might contribute to an improved treatment planning and outcome.

ACKNOWLEDGMENTS

We would like to thank the patients and control participants who agreed to take part in this study. The authors would like to thank Patrick Viout, Lauriane Pini, Claire Costes, and Veronique Gimenez for data acquisition and study logistics, and Lucas Gauer and Olivier Girard for their fruitful discussion on the presented results and/or support at various stages of this project.

FUNDING INFORMATION

This study received funding from the French government under the “Programme Investissements d’Avenir”, Excellence Initiative of Aix-Marseille University—A*MIDEX (AMX-19IET-004), 7TEAMS Chair, EPINOV (ANR-17-RHUS-0004) and the European Union's Horizon 2020 Framework Program (785907 and 945539). Author Roy A. M. Haast was supported by a Marie Skłodowska-Curie Actions Postdoctoral Fellowship (101061988).

CONFLICT OF INTEREST STATEMENT

The authors declare no conflicts of interest.

DATA AVAILABILITY STATEMENT

Code to reproduce this work can be found online (<https://github.com/royhaast/smk-epilepsy-7T-sctx>). The data are not publicly available due to sensitive information that could compromise the privacy of research participants. Nonetheless, anonymized data are available from the corresponding author on reasonable request.

ORCID

Roy A. M. Haast  <https://orcid.org/0000-0001-8543-2467>

Benoit Testud  <https://orcid.org/0000-0003-1444-3702>

Julia Makhlova  <https://orcid.org/0000-0001-7962-2942>

Hugo Dary  <https://orcid.org/0000-0003-0475-5905>

Arnaud Le Troter  <https://orcid.org/0000-0002-7897-9672>

Jean-Philippe Ranjeva  <https://orcid.org/0000-0001-8073-102X>

Fabrice Bartolomei  <https://orcid.org/0000-0002-1678-0297>

Maxime Guye  <https://orcid.org/0000-0002-4435-2257>

REFERENCES

- Aggarwal, M., Li, X., Gröhn, O., & Sierra, A. (2018). Nuclei-specific deposits of iron and calcium in the rat thalamus after status epilepticus revealed with quantitative susceptibility mapping (QSM). *Journal of Magnetic Resonance Imaging*, 47(2), 554–564. <https://doi.org/10.1002/jmri.25777>
- Avants, B. B., Epstein, C. L., Grossman, M., & Gee, J. C. (2008). Symmetric diffeomorphic image registration with cross-correlation: Evaluating automated labeling of elderly and neurodegenerative brain. *Medical Image Analysis*, 12(1), 26–41. <https://doi.org/10.1016/j.media.2007.06.004>
- Avants, B. B., Tustison, N. J., Song, G., Cook, P. A., Klein, A., & Gee, J. C. (2011). A reproducible evaluation of ANTs similarity metric performance in brain image registration. *NeuroImage*, 54(3), 2033–2044. <https://doi.org/10.1016/j.neuroimage.2010.09.025>
- Barron, D. S., Fox, P. M., Laird, A. R., Robinson, J. L., & Fox, P. T. (2012). Thalamic medial dorsal nucleus atrophy in medial temporal lobe epilepsy: A VBM meta-analysis. *NeuroImage: Clinical*, 2, 25–32. <https://doi.org/10.1016/j.nicl.2012.11.004>
- Barron, D. S., Fox, P. T., Pardoe, H., Lancaster, J., Price, L. R., Blackmon, K., Berry, K., Cavazos, J. E., Kuzniecky, R., Devinsky, O., & Thesen, T. (2015). Thalamic functional connectivity predicts seizure laterality in individual TLE patients: Application of a biomarker development strategy. *NeuroImage: Clinical*, 7, 273–280. <https://doi.org/10.1016/j.nicl.2014.08.002>
- Bartolomei, F., Chauvel, P., & Wendling, F. (2008). Epileptogenicity of brain structures in human temporal lobe epilepsy: A quantified study from intracerebral EEG. *Brain*, 131(Pt 7), 1818–1830. <https://doi.org/10.1093/brain/awn111>
- Bartolomei, F., Lagarde, S., Wendling, F., McGonigal, A., Jirsa, V., Guye, M., & Bénar, C. (2017). Defining epileptogenic networks: Contribution of SEEG and signal analysis. *Epilepsia*, 58(7), 1131–1147. <https://doi.org/10.1111/epi.13791>
- Beaulieu, C. (2002). The basis of anisotropic water diffusion in the nervous system—A technical review. *NMR in Biomedicine*, 15(7–8), 435–455. <https://doi.org/10.1002/nbm.782>
- Behrens, T. E. J., Johansen-Berg, H., Woolrich, M. W., Smith, S. M., Wheeler-Kingshott, C. A. M., Boulby, P. A., Barker, G. J., Sillery, E. L., Sheehan, K., Ciccarelli, O., Thompson, A. J., Brady, J. M., & Matthews, P. M. (2003). Non-invasive mapping of connections

- between human thalamus and cortex using diffusion imaging. *Nature Neuroscience*, 6(7), 750–757. <https://doi.org/10.1038/nn1075>
- Bell, P. T., & Shine, J. M. (2016). Subcortical contributions to large-scale network communication. *Neuroscience and Biobehavioral Reviews*, 71, 313–322. <https://doi.org/10.1016/j.neubiorev.2016.08.036>
- Bernhardt, B. C., Bemasconi, N., Kim, H., & Bernasconi, A. (2012). Mapping thalamocortical network pathology in temporal lobe epilepsy. *Neurology*, 78(2), 129–136. <https://doi.org/10.1212/WNL.0b013e31823efcd0d>
- Bernhardt, B. C., Fadaie, F., Vos de Wael, R., Hong, S. J., Liu, M., Guiot, M. C., Rudko, D. A., Bernasconi, A., & Bernasconi, N. (2018). Preferential susceptibility of limbic cortices to microstructural damage in temporal lobe epilepsy: A quantitative T1 mapping study. *NeuroImage*, 182, 294–303. <https://doi.org/10.1016/j.neuroimage.2017.06.002>
- Bertram, E. H., Mangan, P. S., Zhang, D., Scott, C. A., & Williamson, J. M. (2001). The midline thalamus: Alterations and a potential role in limbic epilepsy. *Epilepsia*, 42(8), 967–978. <https://doi.org/10.1046/j.1528-1157.2001.042008967.x>
- Bertram, E. H., Zhang, D., & Williamson, J. M. (2008). Multiple roles of midline dorsal thalamic nuclei in induction and spread of limbic seizures. *Epilepsia*, 49(2), 256–268. <https://doi.org/10.1111/j.1528-1167.2007.01408.x>
- Brun, G., Testud, B., Girard, O. M., Lehmann, P., de Rochefort, L., Besson, P., Massire, A., Ridley, B., Girard, N., Guye, M., Ranjeva, J. P., & le Troter, A. (2022). Automatic segmentation of deep grey nuclei using a high-resolution 7T magnetic resonance imaging atlas-quantification of T1 values in healthy volunteers. *The European Journal of Neuroscience*, 55(2), 438–460. <https://doi.org/10.1111/ejn.15575>
- Chan, S., Erickson, J. K., & Yoon, S. S. (1997). Limbic system abnormalities associated with mesial temporal sclerosis: A model of chronic cerebral changes due to seizures. *Radio Graphics*, 17(5), 1095–1110. <https://doi.org/10.1148/radiographics.17.5.9308104>
- Clascá, F., Rubio-Garrido, P., & Jabaudon, D. (2012). Unveiling the diversity of thalamocortical neuron subtypes. *European Journal of Neuroscience*, 35(10), 1524–1532. <https://doi.org/10.1111/j.1460-9568.2012.08033.x>
- Datta, R., Bacchus, M. K., Kumar, D., Elliott, M. A., Rao, A., Dolui, S., Reddy, R., Banwell, B. L., & Saranathan, M. (2021). Fast automatic segmentation of thalamic nuclei from MP2RAGE acquisition at 7 Tesla. *Magnetic Resonance in Medicine*, 85(5), 2781–2790. <https://doi.org/10.1002/mrm.28608>
- de Curtis, M., Garbelli, R., & Uva, L. (2021). A hypothesis for the role of axon demyelination in seizure generation. *Epilepsia*, 62(3), 583–595. <https://doi.org/10.1111/epi.16824>
- DeLong, M. R., & Wichmann, T. (2007). Circuits and circuit disorders of the basal ganglia. *Archives of Neurology*, 64(1), 20–24. <https://doi.org/10.1001/archneur.64.1.20>
- Drenthen, G. S., Backes, W. H., Rouhl, R. P. W., Vlooswijk, M. C. G., Majoie, M. H. J. M., Hofman, P. A. M., Aldenkamp, A. P., & Jansen, J. F. A. (2018). Structural covariance networks relate to the severity of epilepsy with focal-onset seizures. *NeuroImage: Clinical*, 20, 861–867. <https://doi.org/10.1016/j.nicl.2018.09.023>
- Duyn, J. H. (2018). Studying brain microstructure with magnetic susceptibility contrast at high-field. *NeuroImage*, 168, 152–161. <https://doi.org/10.1016/j.neuroimage.2017.02.046>
- Fattorusso, A., Matricardi, S., Mencaroni, E., Dell'Isola, G. B., di Cara, G., Striano, P., & Verrotti, A. (2021). The pharmaco-resistant epilepsy: An overview on existent and new emerging therapies. *Frontiers in Neurology*, 12, 674483. <https://doi.org/10.3389/fneur.2021.674483>
- Filipescu, C., Lagarde, S., Lambert, I., Pizzo, F., Trébuchon, A., McGonigal, A., Scavarda, D., Carron, R., & Bartolomei, F. (2019). The effect of medial pulvinar stimulation on temporal lobe seizures. *Epilepsia*, 60(4), e25–e30. <https://doi.org/10.1111/epi.14677>
- Fischl, B. (2012). Free surfer. *NeuroImage*, 62(2), 774–781. <https://doi.org/10.1016/j.neuroimage.2012.01.021>
- Galovic, M., van Dooren, V. Q. H., Postma, T. S., Vos, S. B., Caciagli, L., Borzi, G., Cueva Rosillo, J., Vuong, K. A., de Tisi, J., Nachev, P., Duncan, J. S., & Koepp, M. J. (2019). Progressive cortical thinning in patients with focal epilepsy. *JAMA Neurology*, 76(10), 1230–1239. <https://doi.org/10.1001/jamaneurol.2019.1708>
- Gibson, E. M., Purger, D., Mount, C. W., Goldstein, A. K., Lin, G. L., Wood, L. S., Inema, I., Miller, S. E., Bieri, G., Zuchero, J. B., Barres, B. A., Woo, P. J., Vogel, H., & Monje, M. (2014). Neuronal activity promotes oligodendrogenesis and adaptive myelination in the mammalian brain. *Science*, 344(6183), 1252304. <https://doi.org/10.1126/science.1252304>
- Girard, O., De Rochefort, L., Guye, M., Ranjeva, J.-P., & Troter, A. L. (2021). 7TAMlbrain. <https://doi.org/10.18112/OPENNEURO.DS003967.V1.0.0>
- Goubran, M., Hammond, R. R., de Ribaupierre, S., Burneo, J. G., Mirsattari, S., Steven, D. A., Parrent, A. G., Peters, T. M., & Khan, A. R. (2015). Magnetic resonance imaging and histology correlation in the neocortex in temporal lobe epilepsy. *Annals of Neurology*, 77(2), 237–250. <https://doi.org/10.1002/ana.24318>
- Guye, M., Régis, J., Tamura, M., Wendling, F., McGonigal, A., Chauvel, P., & Bartolomei, F. (2006). The role of corticothalamic coupling in human temporal lobe epilepsy. *Brain*, 129(Pt 7), 1917–1928. <https://doi.org/10.1093/brain/awl151>
- Haast, R. A. M., Ivanov, D., & Uludağ, K. (2018). The impact of B1+ correction on MP2RAGE cortical T1 and apparent cortical thickness at 7T. *Human Brain Mapping*, 39(6), 2412–2425. <https://doi.org/10.1002/hbm.24011>
- Haast, R. A. M., Lau, J. C., Ivanov, D., Menon, R. S., Uludağ, K., & Khan, A. R. (2021). Effects of MP2RAGE B1+ sensitivity on inter-site T1 reproducibility and hippocampal morphometry at 7T. *NeuroImage*, 224, 117373. <https://doi.org/10.1016/j.neuroimage.2020.117373>
- Hughes, E. J., Bond, J., Svrckova, P., Makropoulos, A., Ball, G., Sharp, D. J., Edwards, A. D., Hajnal, J. V., & Counsell, S. J. (2012). Regional changes in thalamic shape and volume with increasing age. *NeuroImage*, 63(3), 1134–1142. <https://doi.org/10.1016/j.neuroimage.2012.07.043>
- Isnard, J., Taussig, D., Bartolomei, F., Bourdillon, P., Catenoux, H., Chassoux, F., Chipaux, M., Clémenceau, S., Colnat-Coulbois, S., Denuelle, M., Derrey, S., Devaux, B., Dorfmueller, G., Gilard, V., Guenot, M., Job-Chapron, A. S., Landré, E., Lebas, A., Maillard, L., ... Sauleau, P. (2018). French guidelines on stereoelectroencephalography (SEEG). *Neurophysiologie Clinique*, 48(1), 5–13. <https://doi.org/10.1016/j.neucli.2017.11.005>
- Jones, E. G. (2009). Synchrony in the interconnected circuitry of the thalamus and cerebral cortex. *Annals of the New York Academy of Sciences*, 1157, 10–23. <https://doi.org/10.1111/j.1749-6632.2009.04534.x>
- Kai, J., Khan, A. R., Haast, R. A., & Lau, J. C. (2022). Mapping the subcortical connectome using in vivo diffusion MRI: Feasibility and reliability. *NeuroImage*, 262, 119553. <https://doi.org/10.1016/j.neuroimage.2022.119553>
- Kashyap, S. (2021). *srikash/presurfer: ondu*. <https://doi.org/10.5281/zenodo.4626841>
- Kashyap, S., Ivanov, D., Havlicek, M., Huber, L., Poser, B. A., & Uludağ, K. (2021). Sub-millimetre resolution laminar fMRI using arterial spin labeling in humans at 7 T. *PLoS One*, 16(4), e0250504. <https://doi.org/10.1371/journal.pone.0250504>
- Keller, S. S., O'Muircheartaigh, J., Traynor, C., Towgood, K., Barker, G. J., & Richardson, M. P. (2014). Thalamotemporal impairment in temporal lobe epilepsy: A combined MRI analysis of structure, integrity, and connectivity. *Epilepsia*, 55(2), 306–315. <https://doi.org/10.1111/epi.12520>
- Keller, S. S., Richardson, M. P., Schoene-Bake, J. C., O'Muircheartaigh, J., Elkammos, S., Kreilkamp, B., Goh, Y. Y., Marson, A. G., Elger, C., & Weber, B. (2015). Thalamotemporal alteration and postoperative seizures in temporal lobe epilepsy. *Annals of Neurology*, 77(5), 760–774. <https://doi.org/10.1002/ana.24376>

- Khan, A. R., Goubran, M., de Ribaupierre, S., Hammond, R. R., Burneo, J. G., Parrent, A. G., & Peters, T. M. (2014). Quantitative relaxometry and diffusion MRI for lateralization in MTS and non-MTS temporal lobe epilepsy. *Epilepsy Research*, 108(3), 506–516. <https://doi.org/10.1016/j.eplepsyres.2013.12.012>
- Khan, A. R., Hiebert, N. M., Vo, A., Wang, B. T., Owen, A. M., Seergobin, K. N., & MacDonald, P. A. (2019). Biomarkers of Parkinson's disease: Striatal sub-regional structural morphometry and diffusion MRI. *NeuroImage: Clinical*, 21, 101597. <https://doi.org/10.1016/j.nicl.2018.11.007>
- Kirschner, M., Shafiei, G., Markello, R. D., Makowski, C., Talpalari, A., Hodzic-Santor, B., Devenyi, G. A., Paquola, C., Bernhardt, B. C., Lepage, M., Chakravarty, M. M., Dagher, A., & Mišić, B. (2020). Latent clinical-anatomical dimensions of schizophrenia. *Schizophrenia Bulletin*, 46(6), 1426–1438. <https://doi.org/10.1093/schbul/sbaa097>
- Knowles, J. K., Xu, H., Soane, C., Batra, A., Saucedo, T., Frost, E., Tam, L. T., Fraga, D., Ni, L., Villar, K., Talmi, S., Huguenard, J. R., & Monje, M. (2022). Maladaptive myelination promotes generalized epilepsy progression. *Nature Neuroscience*, 25(5), 596–606. <https://doi.org/10.1038/s41593-022-01052-2>
- Kwan, P., Arzimanoglou, A., Berg, A. T., Brodie, M. J., Allen Hauser, W., Mathern, G., Moshé, S. L., Puccia, E., Wiebe, S., & French, J. (2010). Definition of drug resistant epilepsy: Consensus proposal by the ad hoc task force of the ILAE commission on therapeutic strategies. *Epilepsia*, 51(6), 1069–1077. <https://doi.org/10.1111/j.1528-1167.2009.02397.x>
- Lambert, C., Simon, H., Colman, J., & Barrick, T. R. (2017). Defining thalamic nuclei and topographic connectivity gradients in vivo. *NeuroImage*, 158, 466–479. <https://doi.org/10.1016/j.neuroimage.2016.08.028>
- Larivière, S., Bernasconi, A., Bernasconi, N., & Bernhardt, B. C. (2021). Connectome biomarkers of drug-resistant epilepsy. *Epilepsia*, 62(1), 6–24. <https://doi.org/10.1111/epi.16753>
- Larivière, S., Rodríguez-Cruces, R., Royer, J., Caligiuri, M. E., Gambardella, A., Concha, L., Keller, S. S., Cendes, F., Yasuda, C., Bonilha, L., Gleichgerrcht, E., Focke, N. K., Domin, M., von Podewills, F., Langner, S., Rummel, C., Wiest, R., Martin, P., Kotikalapudi, R., ... Bernhardt, B. C. (2020). Network-based atrophy modeling in the common epilepsies: A worldwide ENIGMA study. *Science Advances*, 6(47), eabc 6457. <https://doi.org/10.1126/sciadv.abc6457>
- Larivière, S., Royer, J., Rodríguez-Cruces, R., Paquola, C., Caligiuri, M. E., Gambardella, A., Concha, L., Keller, S. S., Cendes, F., Yasuda, C. L., Bonilha, L., Gleichgerrcht, E., Focke, N. K., Domin, M., von Podewills, F., Langner, S., Rummel, C., Wiest, R., Martin, P., ... Bernhardt, B. C. (2022). Structural network alterations in focal and generalized epilepsy assessed in a worldwide ENIGMA study follow axes of epilepsy risk gene expression. *Nature Communications*, 13, 4320. <https://doi.org/10.1038/s41467-022-31730-5>
- Le Ster, C., Grant, A., Van de Moortele, P. F., Monreal-Madrigal, A., Adriany, G., Vignaud, A., Mauconduit, F., Rabrait-Lerman, C., Poser, B. A., Uğurbil, K., & Boulant, N. (2022). Magnetic field strength dependent SNR gain at the center of a spherical phantom and up to 11.7T. *Magnetic Resonance in Medicine*, 88(5), 2131–2138. <https://doi.org/10.1002/mrm.29391>
- Lee, H. M., Fadaie, F., Gill, R., Caldairou, B., Sziklas, V., Crane, J., Hong, S. J., Bernhardt, B. C., Bernasconi, A., & Bernasconi, N. (2022). Decomposing MRI phenotypic heterogeneity in epilepsy: A step towards personalized classification. *Brain*, 145(3), 897–908. <https://doi.org/10.1093/brain/awab425>
- Leek, N. J., Neason, M., Kreilkamp, B. A. K., de Bezenac, C., Ziso, B., Elkomos, S., Das, K., Marson, A. G., & Keller, S. S. (2021). Thalamohippocampal atrophy in focal epilepsy of unknown cause at the time of diagnosis. *European Journal of Neurology*, 28(2), 367–376. <https://doi.org/10.1111/ene.14565>
- Lenglet, C., Abosch, A., Yacoub, E., De Martino, F., Sapiro, G., & Harel, N. (2012). Comprehensive in vivo mapping of the human basal ganglia and thalamic connectome in individuals using 7T MRI. *PLoS One*, 7(1), e29153. <https://doi.org/10.1371/journal.pone.0029153>
- Loring, D. W., Meador, K. J., & Lee, G. P. (2004). Determinants of quality of life in epilepsy. *Epilepsy & Behavior*, 5(6), 976–980. <https://doi.org/10.1016/j.yebeh.2004.08.019>
- Marcus, D. S., Harwell, J., Olsen, T., Hodge, M., Glasser, M. F., Prior, F., Jenkinson, M., Laumann, T., Curtiss, S. W., & van Essen, D. (2011). Informatics and data mining tools and strategies for the human connectome project. *Frontiers in Neuroinformatics*, 5, 4. <https://doi.org/10.3389/fninf.2011.00004>
- Marques, J. P., & Gruetter, R. (2013). New developments and applications of the MP2RAGE sequence—Focusing the contrast and high spatial resolution R1 mapping. *PLoS One*, 8(7), e69294. <https://doi.org/10.1371/journal.pone.0069294>
- Marques, J. P., Kober, T., Krueger, G., van der Zwaag, W., Van de Moortele, P. F., & Gruetter, R. (2010). MP2RAGE, a self bias-field corrected sequence for improved segmentation and. *NeuroImage*, 49(2), 1271–1281. <https://doi.org/10.1016/j.neuroimage.2009.10.002>
- Mathur, B. N. (2014). The claustrum in review. *Frontiers in Systems Neuroscience*, 8, 48. <https://doi.org/10.3389/fnysys.2014.00048>
- McIntosh, A. R., & Mišić, B. (2013). Multivariate statistical analyses for neuroimaging data. *Annual Review of Psychology*, 64, 499–525. <https://doi.org/10.1146/annurev-psych-113011-143804>
- Mezer, A., Yeatman, J. D., Stikov, N., Kay, K. N., Cho, N. J., Dougherty, R. F., Perry, M. L., Parvizi, J., Hua, L. H., Butts-Pauly, K., & Wandell, B. A. (2013). Quantifying the local tissue volume and composition in individual brains with magnetic resonance imaging. *Nature Medicine*, 19(12), 1667–1672. <https://doi.org/10.1038/nm.3390>
- Morel, A., Magnin, M., & Jeanmonod, D. (1997). Multiarchitectonic and stereotactic atlas of the human thalamus. *The Journal of Comparative Neurology*, 387(4), 588–630. [https://doi.org/10.1002/\(sici\)1096-9861\(19971103\)387:4<588::aid-cne8>3.0.co;2-z](https://doi.org/10.1002/(sici)1096-9861(19971103)387:4<588::aid-cne8>3.0.co;2-z)
- Natsume, J., Bernasconi, N., Andermann, F., & Bernasconi, A. (2003). MRI volumetry of the thalamus in temporal, extratemporal, and idiopathic generalized epilepsy. *Neurology*, 60(8), 1296–1300. <https://doi.org/10.1212/01.wnl.0000058764.34968.c2>
- Nieuwenhuys, R. (2013). The myeloarchitectonic studies on the human cerebral cortex of the Vogt-Vogt school, and their significance for the interpretation of functional neuroimaging data. *Brain Structure & Function*, 218(2), 303–352. <https://doi.org/10.1007/s00429-012-0460-z>
- Opheim, G., van der Kolk, A., Bloch, K. M., Colon, A. J., Davis, K. A., Henry, T. R., Jansen, J. F. A., Jones, S. E., Pan, J. W., Rössler, K., Stein, J. M., Strandberg, M. C., Tractnig, S., Moortele, P-FV. de., Vargas, M. I., Wang, I., Bartolomei, F., Bernasconi, N., Bernasconi, A., Bernhardt, B., ... Guye, M. (2020). 7T epilepsy task force consensus recommendations on the use of 7T in clinical practice. *Neurology*, 96(7), 327–341. <https://doi.org/10.1212/WNL.00000000000011413>
- Pizzo, F., Roehri, N., Giusiano, B., Lagarde, S., Carron, R., Scavarda, D., McGonigal, A., Filipescu, C., Lambert, I., Bonini, F., Trebuchon, A., Bénar, C. G., & Bartolomei, F. (2021). The ictal signature of thalamus and basal ganglia in focal epilepsy: A SEEG study. *Neurology*, 96(2), e280–e293. <https://doi.org/10.1212/WNL.00000000000011003>
- Pohmann, R., Speck, O., & Scheffler, K. (2016). Signal-to-noise ratio and MR tissue parameters in human brain imaging at 3, 7, and 9.4 Tesla using current receive coil arrays. *Magnetic Resonance in Medicine*, 75(2), 801–809. <https://doi.org/10.1002/mrm.25677>
- Raamana, P. R. (2020). *Conquering confounds and covariates in machine learning with the python library confounds*. <https://doi.org/10.5281/zenodo.3701528>
- Rodríguez-Cruces, R., Bernhardt, B. C., & Concha, L. (2020). Multidimensional associations between cognition and connectome organization in temporal lobe epilepsy. *NeuroImage*, 213, 116706. <https://doi.org/10.1016/j.neuroimage.2020.116706>

- Rodríguez-Cruces, R., Royer, J., Larivière, S., Bassett, D. S., Caciagli, L., & Bernhardt, B. C. (2022). Multimodal connectome biomarkers of cognitive and affective dysfunction in the common epilepsies. *Network Neuroscience*, 6(2), 320–338. https://doi.org/10.1162/netn_a_00237
- Rooney, W. D., Johnson, G., Li, X., Cohen, E. R., Kim, S. G., Ugurbil, K., & Springer, C. S. (2007). Magnetic field and tissue dependencies of human brain longitudinal 1H2O relaxation in vivo. *Magnetic Resonance in Medicine*, 57(2), 308–318. <https://doi.org/10.1002/mrm.21122>
- Rosenberg, D. S., Mauguière, F., Demarquay, G., Ryvlin, P., Isnard, J., Fischer, C., Guénot, M., & Magnin, M. (2006). Involvement of medial pulvinar thalamic nucleus in human temporal lobe seizures. *Epilepsia*, 47(1), 98–107. <https://doi.org/10.1111/j.1528-1167.2006.00375.x>
- Rüber, T., David, B., Lüchters, G., Nass, R. D., Friedman, A., Surges, R., Stöcker, T., Weber, B., Deichmann, R., Schlaug, G., Hattngen, E., & Elger, C. E. (2018). Evidence for peri-ictal blood–brain barrier dysfunction in patients with epilepsy. *Brain*, 141(10), 2952–2965. <https://doi.org/10.1093/brain/awy242>
- Sherman, S. M. (2016). Thalamus plays a central role in ongoing cortical functioning. *Nature Neuroscience*, 19(4), 533–541. <https://doi.org/10.1038/nn.4269>
- Shine, J. M. (2021). The thalamus integrates the macrosystems of the brain to facilitate complex, adaptive brain network dynamics. *Progress in Neurobiology*, 199, 101951. <https://doi.org/10.1016/j.pneurobio.2020.101951>
- Sinha, N., Peternell, N., Schroeder, G. M., Tisi, J., Vos, S. B., Winston, G. P., Duncan, J. S., Wang, Y., & Taylor, P. N. (2021). Focal to bilateral tonic-clonic seizures are associated with widespread network abnormality in temporal lobe epilepsy. *Epilepsia*, 62(3), 729–741. <https://doi.org/10.1111/epi.16819>
- Sisodiya, S. M., Whelan, C. D., Hatton, S. N., Huynh, K., Altmann, A., Rytten, M., Vezzani, A., Caligiuri, M. E., Labate, A., Gambardella, A., Ives-Deliperi, V., Meletti, S., Munsell, B. C., Bonilha, L., Tondelli, M., Rebsamen, M., Rummel, C., Vaudano, A. E., Wiest, R., ... Zhang, G. (2022). The ENIGMA–Epilepsy working group: Mapping disease from large data sets. *Human Brain Mapping*, 43(1), 113–128. <https://doi.org/10.1002/hbm.25037>
- Stüber, C., Morawski, M., Schäfer, A., Labadie, C., Wähner, M., Leuze, C., Streicher, M., Barapatre, N., Reimann, K., Geyer, S., Spemann, D., & Turner, R. (2014). Myelin and iron concentration in the human brain: A quantitative study of MRI contrast. *NeuroImage*, 93, 95–106. <https://doi.org/10.1016/j.neuroimage.2014.02.026>
- Su, J. H., Thomas, F. T., Kasoff, W. S., Tourdias, T., Choi, E. Y., Rutt, B. K., & Saranathan, M. (2019). Thalamus optimized multi atlas segmentation (THOMAS): Fast, fully automated segmentation of thalamic nuclei from structural MRI. *NeuroImage*, 194, 272–282. <https://doi.org/10.1016/j.neuroimage.2019.03.021>
- Tang, Y., Su, T. Y., Choi, J. Y., Hu, S., Wang, X., Sakaie, K., Murakami, H., Alexopoulos, A., Griswold, M., Jones, S., Najm, I., Ma, D., & Wang, Z. I. (2022). Characterizing thalamic and basal ganglia nuclei in medically intractable focal epilepsy by MR fingerprinting. *Epilepsia*, 63(8), 1998–2010. <https://doi.org/10.1111/epi.17318>
- Trattng, S., Springer, E., Bogner, W., Hangel, G., Strasser, B., Dymerska, B., Cardoso, P. L., & Robinson, S. D. (2018). Key clinical benefits of neuroimaging at 7T. *NeuroImage*, 168, 477–489. <https://doi.org/10.1016/j.neuroimage.2016.11.031>
- Wang, H., Suh, J. W., Das, S. R., Pluta, J. B., Craige, C., & Yushkevich, P. A. (2013). Multi-atlas segmentation with joint label fusion. *IEEE Transactions on Pattern Analysis and Machine Intelligence*, 35(3), 611–623. <https://doi.org/10.1109/TPAMI.2012.143>
- Ward, R. J., Zucca, F. A., Duyn, J. H., Crichton, R. R., & Zecca, L. (2014). The role of iron in brain ageing and neurodegenerative disorders. *The Lancet Neurology*, 13(10), 1045–1060. [https://doi.org/10.1016/S1473-4422\(14\)70117-6](https://doi.org/10.1016/S1473-4422(14)70117-6)
- Whelan, C. D., Altmann, A., Botia, J. A., Jahanshad, N., Hibar, D. P., Absil, J., Alhusaini, S., Alvim, M. K. M., Auvinen, P., Bartolini, E., Berge, F. P. G., Bernardes, T., Blackmon, K., Braga, B., Caligiuri, M. E., Calvo, A., Carr, S. J., Chen, J., Chen, S., ... Sisodiya, S. M. (2018). Structural brain abnormalities in the common epilepsies assessed in a worldwide ENIGMA study. *Brain*, 141(2), 391–408. <https://doi.org/10.1093/brain/awx341>
- Wirsih, J., Perry, A., Ridley, B., Proix, T., Golos, M., Bénar, C., Ranjeva, J. P., Bartolomei, F., Breakspear, M., Jirsa, V., & Guye, M. (2016). Whole-brain analytic measures of network communication reveal increased structure–function correlation in right temporal lobe epilepsy. *NeuroImage: Clinical*, 11, 707–718. <https://doi.org/10.1016/j.nicl.2016.05.010>

SUPPORTING INFORMATION

Additional supporting information can be found online in the Supporting Information section at the end of this article.

How to cite this article: Haast, R. A. M., Testud, B., Makhalova, J., Dary, H., Cabane, A., Le Troter, A., Ranjeva, J.-P., Bartolomei, F., & Guye, M. (2023). Multi-scale structural alterations of the thalamus and basal ganglia in focal epilepsy using 7T MRI. *Human Brain Mapping*, 44(13), 4754–4771. <https://doi.org/10.1002/hbm.26414>